SUPPLEMENTAL MATERIAL

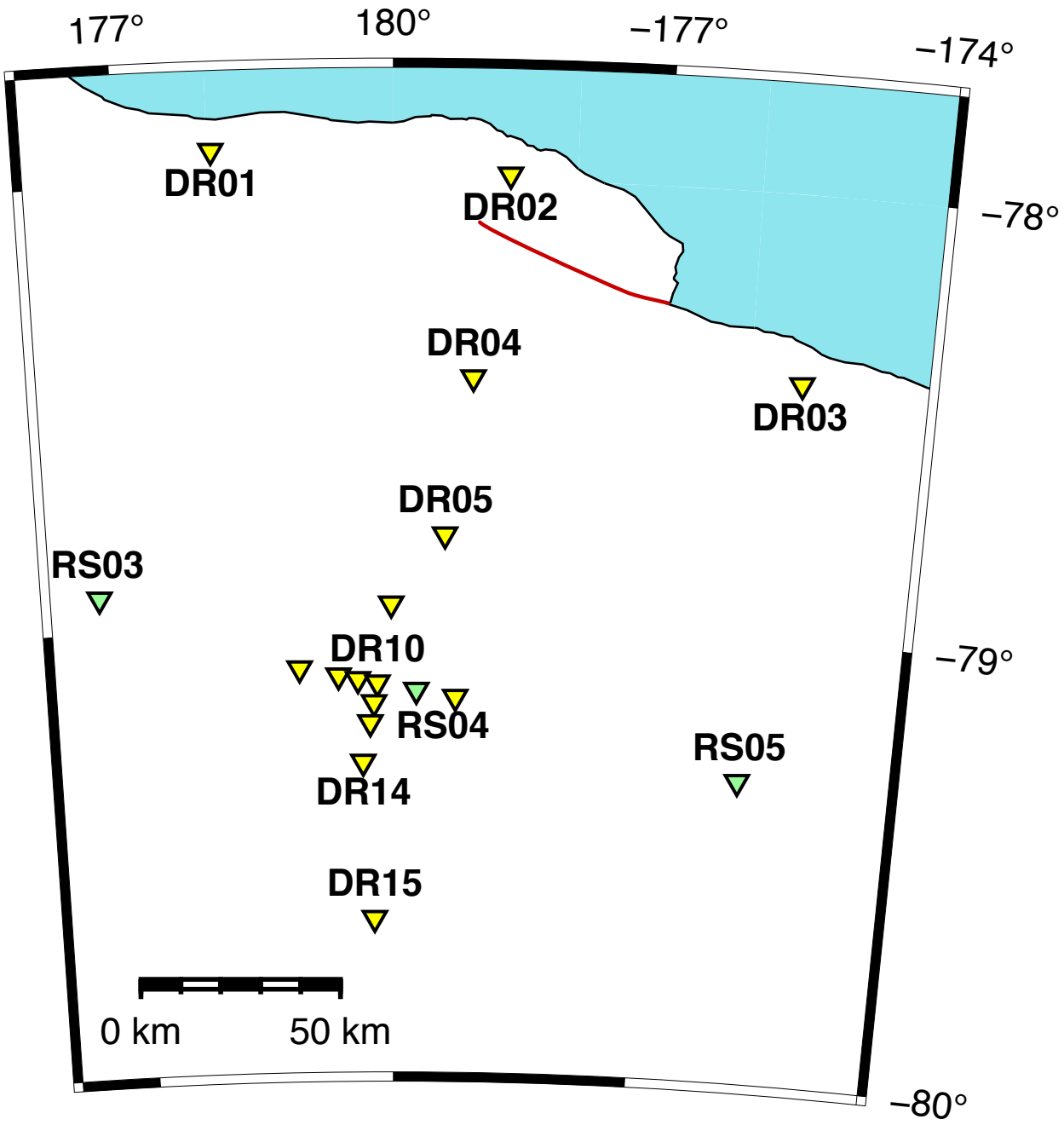

Fig. S1. Map of RIS ice front stations. The rift bounding the semi-detached Nascent Iceberg is denoted in red (adapted from LeDoux and others (2017)). Station coordinates for DR01–DR03 have been manually shifted to accommodate the discrepancy between BEDMAP2 data and the current location of the RIS ice front and are presented for illustrative purposes only. DR stations (yellow) sampled at 200 Hz; RS stations (green) sampled at 100 Hz, except for RS04 which was also 200 Hz.

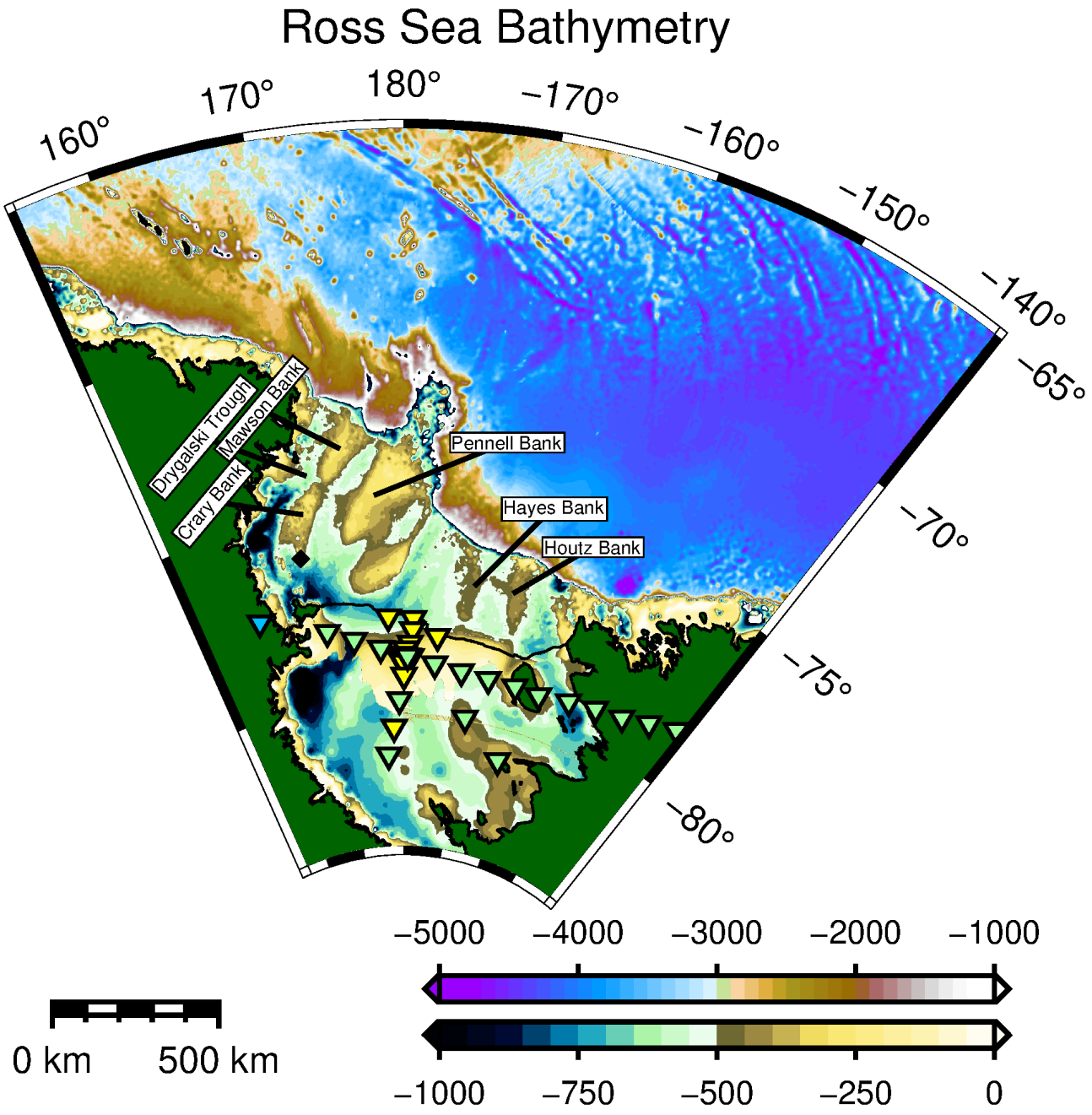

Fig. S2. High-contrast bathymetry for the Ross Sea Embayment (bottom color scale) and the adjacent continental slope and oceanic basin (top color scale). Depths are given in meters.

Table S1. Wave modes of the Ross Ice Shelf. Velocities and periods, unless otherwise noted, are calculated with ice thickness $h = 330$ m, water thickness $h = 440$ m, P-wave velocity $\alpha_i = 3.87$ km s^{-1}, S-wave velocity $\beta_i = 1.875$ km s^{-1} [a], and acoustic velocity $\alpha_w = 1.50$ km s^{-1}.

Wave Type	Wavelength Limits	Bandpass (s)	Velocity (km s^{-1})	HOV (dB)	Notes
Flexural-Gravity	$< 11km$[f]	$\sim$1 – 150	< 0.07[b,d]	(−)	Transitions to pure gravity modes at very long periods. Transitions to water-coupled A0 Lamb at short periods.
Lamb, A_0	$\frac{h}{2}$ – $2(h+H)$	0.1 – 1.0	$\leq \alpha_w$[d]	(−)	Transitions to Rayleigh wave at short periods.
Lamb, S_0	$\frac{h}{2} - \infty$	0.1 – ∞	3.2[b,c]	(+)	Insensitive to ice/water interface.[b] Transitions to Rayleigh wave at short periods.
Rayleigh	$\frac{1}{\infty}$ – $\frac{h}{2}$	$\frac{1}{\infty}$ – 0.1	1.75[c]	(−)	Couples with both plate surfaces at long periods. Dispersive for periods < 0.02 s; i.e., confined to firn layer.[a]
Love, n = 1	$\approx 5.0h$	0.33	5.0[c]	(+)	For $p = 0.2$ s km^{-1}.
Crary, n = 1	$\approx 0.97h$	0.15	2.1[e]	(+)	For $\theta_c = 29°$.

[a] Empirical value from Diez and others (2016).
[b] Empirical value from Chen and others (2018).
[c] Theoretical value from Viktorov (1967).
[d] Theoretical value from Robinson (1983).
[e] Theoretical value from Crary (1954).
[f] Flexural-gravity wavelength from Lipovsky (2018).

787

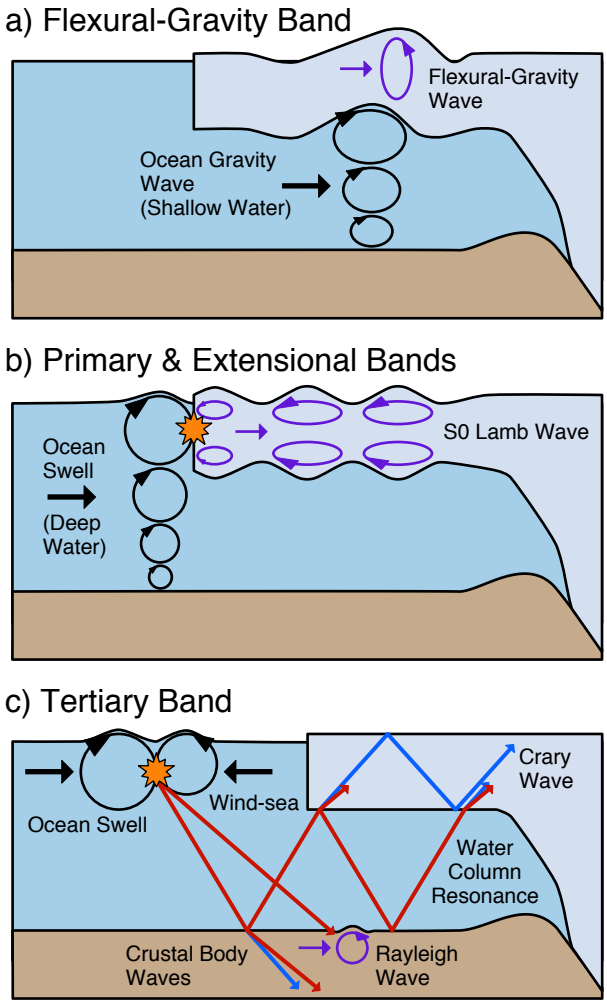

Fig. S3. Schematic of the ocean-forced wave modes endemic to the Ross Ice Shelf (Table S1), categorized by the period bands (Table 1) for which these modes are most dominant (but not necessarily exclusive). **a)** A long period (<150 s) flexural-gravity wave (i.e., a buoyancy-coupled asymmetric mode (A0) Lamb wave) propagating at a higher phase velocity than its progenating ocean gravity wave. At ultra long periods (≫150 s), the elastic properties of the ice shelf are negligible and particle motion is expected to become prograde and in-phase with the sub-shelf ocean waves. At short periods (<1 s for the RIS), buoyancy is insignificant in comparison to the elastic restoring force and this wavemode is entirely described by the A0 Lamb wave equation (Viktorov, 1967; Robinson, 1983; Chen and others, 2018). **b)** S0 Lamb waves in the Primary and Extensional bands are excited by the impact of ocean swell against the ice front; swell energy also propagates into the sub-shelf cavity and excites intermediate period (10–30 s) flexural-gravity waves. **c)** Potential mechanism for the generation of acoustic waves via nonlinear wave-wave interaction of ocean swell and opposing wind-sea (e.g., Ardhuin and Herbers, 2013). These acoustic phases can couple into crustal body and surface modes and may also propagate into the sub-shelf cavity, where high reflection coefficients at the ice/water and water/seafloor interfaces promote strong resonances within the ice shelf and water column. Rayleigh waves arising from this process may be responsible for similar lake-ice-modulated microseism signals (Xu and others, 2017; Anthony and others, 2018; Smalls and others, 2019).

Table S2. Number of days per year for which DRxx station mean band power (M) (based on the daily median power) approached the band-averages for the New Low and New High Noise Models (NLNM and NHNM, respectively) (Peterson, 1993). The left column tallies the number of days such that M $\leq$ NLNM+2 dB; the right column tallies the number of days such that M $\geq$ NHNM−2 dB. Lo/Hi days were counted across the full deployment and scaled to 365 days.

Station		Tertiary (0.4–4.0 s)		Secondary (5–10 s)		Primary (10–20 s)		Extensional (20–50 s)		Flex-Grav (50–100 s)	
DR01	HHZ	0	10	0	124	0	49	0	365	0	365
	HHN	35	5	0	94	1	39	0	365	0	365
	HHE	50	2	0	90	1	22	0	365	0	365
DR02	HHZ	0	19	0	352	0	67	0	365	0	365
	HHN	0	14	0	136	0	53	0	365	0	365
	HHE	1	9	0	141	0	51	0	365	0	365
DR03	HHZ	0	21	0	109	0	27	0	365	0	365
	HHN	14	6	0	71	3	21	0	365	0	365
	HHE	19	5	0	71	0	16	0	365	0	365
DR04	HHZ	0	0	0	66	0	2	0	344	0	344
	HHN	194	0	0	57	2	0	0	344	0	344
	HHE	192	0	2	52	2	0	0	344	0	344
DR05	HHZ	0	0	0	41	0	0	0	365	0	365
	HHN	232	0	3	44	3	0	0	365	0	365
	HHE	222	0	7	36	2	0	0	360	0	365
DR06	HHZ	0	0	0	8	0	0	0	275	0	365
	HHN	226	0	4	42	2	0	0	360	0	365
	HHE	224	0	6	27	4	0	0	336	0	365
DR07	HHZ	0	0	0	2	0	0	0	150	0	365
	HHN	223	0	5	42	1	0	0	352	0	365
	HHE	210	0	4	37	3	0	0	290	0	365
DR08	HHZ	0	0	0	1	0	0	0	116	0	365
	HHN	224	0	8	37	2	0	0	351	0	365
	HHE	205	0	9	28	4	0	0	286	0	365
DR09	HHZ	0	0	0	1	0	0	0	100	0	365
	HHN	227	0	10	35	5	0	0	350	0	365
	HHE	227	0	10	24	5	0	0	289	0	365
DR10	HHZ	0	0	0	1	0	0	0	110	0	365
	HHN	228	0	7	35	4	0	0	351	0	365
	HHE	227	0	10	20	5	0	0	294	0	365
DR11	HHZ	0	0	0	1	0	0	0	157	0	365
	HHN	224	0	12	31	5	0	0	354	0	365
	HHE	207	0	13	18	6	0	0	301	0	365
DR12	HHZ	0	0	0	1	0	0	0	88	0	365
	HHN	219	0	5	29	4	0	0	351	0	365
	HHE	214	0	9	17	4	0	0	296	0	365
DR13	HHZ	0	0	0	0	0	0	0	69	0	365
	HHN	222	0	5	36	4	0	0	353	0	365
	HHE	219	0	10	13	5	0	0	291	0	365
DR14	HHZ	0	0	0	0	0	0	0	49	0	365
	HHN	213	0	11	21	0	0	0	289	0	365
	HHE	192	0	19	6	5	0	0	212	0	365
DR15	HHZ	0	0	0	0	0	0	0	0	0	353
	HHN	209	0	15	6	5	0	0	248	0	365
	HHE	202	0	30	1	8	0	0	134	0	352
DR16	HHZ	0	0	0	0	0	0	0	0	0	0
	HHN	250	0	118	0	23	0	0	19	0	24
	HHE	242	0	141	0	24	0	0	1	0	2

Table S3. Continuation of Table S2 for RSxx stations.

Station		Tertiary (0.4–4.0 s)		Secondary (5–10 s)		Primary (10–20 s)		Extensional (20–50 s)		Flex-Grav (50–100 s)	
RS01	HHZ	0	0	0	44	0	1	0	365	0	365
	HHN	189	0	0	60	0	0	0	365	0	365
	HHE	193	0	0	56	0	0	0	360	0	365
RS02	HHZ	0	0	0	27	0	5	0	359	0	365
	HHN	208	0	0	56	1	0	0	364	0	365
	HHE	180	0	2	44	0	0	0	328	0	365
RS03	HHZ	0	0	0	7	0	7	0	215	0	365
	HHN	212	0	3	52	2	0	0	352	0	365
	HHE	118	0	7	41	1	0	0	319	0	365
RS04	HHZ	0	0	0	2	0	0	0	168	0	365
	HHN	210	0	8	34	3	0	0	353	0	365
	HHE	185	0	11	16	6	0	0	295	0	365
RS05	HHZ	0	0	0	4	0	0	0	205	0	365
	HHN	234	0	27	13	11	0	0	356	0	365
	HHE	229	0	34	7	7	0	0	305	0	365
RS06	HHZ	0	0	0	0	0	0	0	56	0	365
	HHN	229	0	62	3	31	0	0	272	0	365
	HHE	232	0	40	2	15	0	0	265	0	365
RS07	HHZ	0	0	0	1	0	0	0	19	0	365
	HHN	185	0	29	0	17	0	0	116	0	365
	HHE	87	0	19	0	4	0	0	76	0	365
RS08	HHZ	0	0	0	0	0	0	0	0	0	0
	HHN	1	0	0	0	0	0	0	0	0	0
	HHE	1	0	0	0	0	0	0	0	0	0
RS09	HHZ	17	0	17	0	17	0	17	0	17	0
	HHN	17	0	17	0	17	0	17	0	17	47
	HHE	17	0	17	0	17	0	17	0	17	0
RS10	HHZ	0	0	0	0	0	0	0	0	0	0
	HHN	5	0	0	3	0	0	0	116	0	236
	HHE	108	0	0	3	0	0	0	133	0	82
RS11	HHZ	0	0	0	0	0	0	0	0	0	0
	HHN	0	0	0	0	0	0	0	70	0	158
	HHE	0	0	0	0	0	0	0	56	0	141
RS12	HHZ	0	0	0	0	0	0	0	0	0	0
	HHN	0	0	0	0	0	0	0	0	0	1
	HHE	0	0	0	0	0	0	0	0	0	0
RS13	HHZ	0	0	0	0	0	0	0	0	0	0
	HHN	0	0	0	0	0	0	0	46	0	116
	HHE	0	0	0	0	0	0	0	59	0	116
RS14	HHZ	0	0	0	0	0	0	0	0	0	0
	HHN	0	0	0	0	0	0	0	73	0	142
	HHE	0	0	0	0	0	0	0	69	0	112
RS15	HHZ	0	0	0	0	0	0	0	0	0	0
	HHN	239	0	169	0	25	0	0	23	0	258
	HHE	250	0	131	0	9	0	0	2	0	120
RS16	HHZ	0	0	0	0	0	0	0	0	0	0
	HHN	234	0	48	0	11	0	0	61	0	282
	HHE	228	0	72	0	9	0	0	27	0	17
RS17	HHZ	0	0	0	0	0	0	0	0	0	0
	HHN	0	0	0	0	0	3	0	0	0	0
	HHE	0	0	0	0	0	2	0	0	0	0
RS18	HHZ	0	0	0	0	0	5	0	0	0	0
	HHN	260	0	162	0	7	0	0	4	0	15
	HHE	259	0	170	0	8	0	0	0	0	6

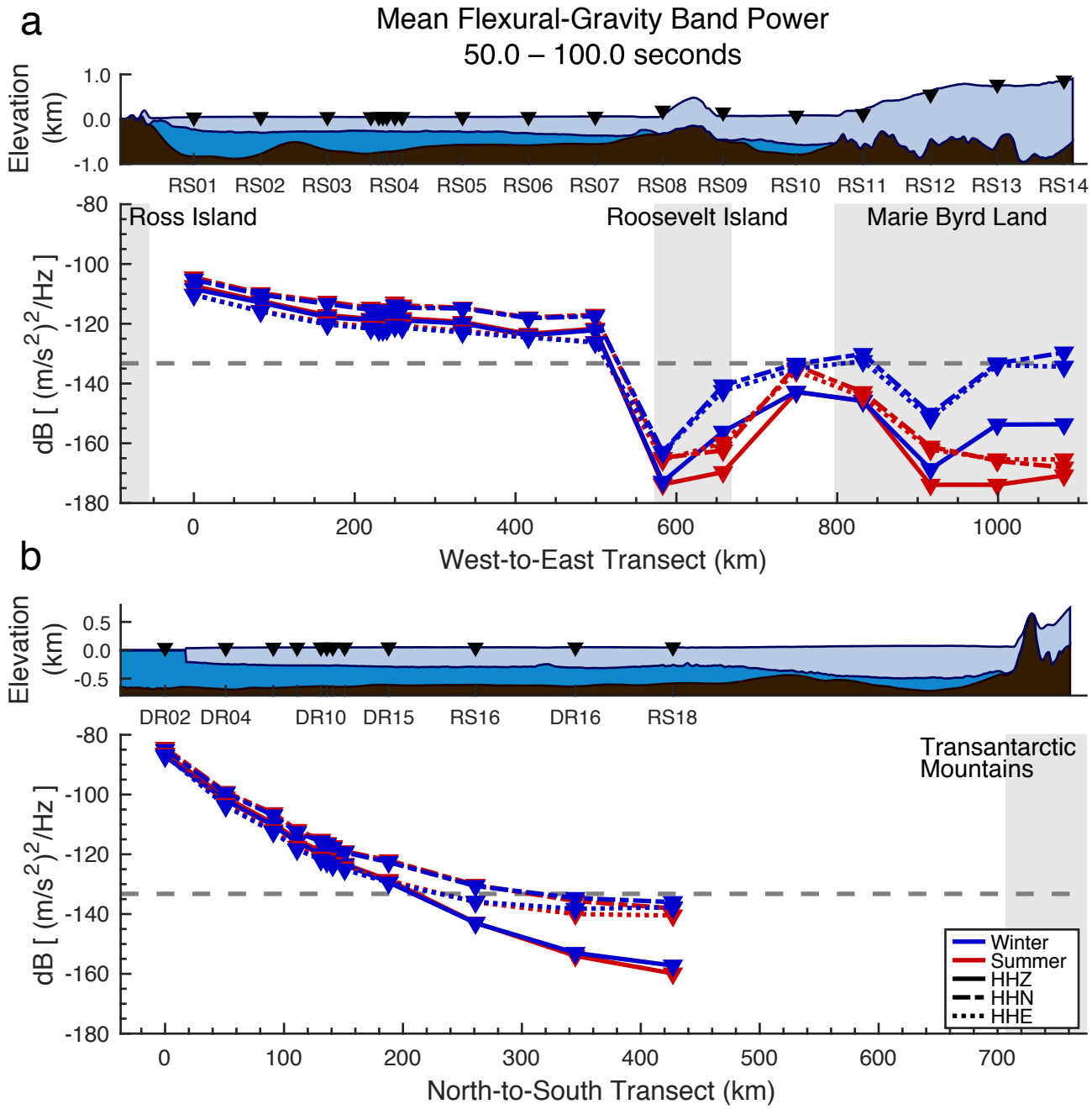

Fig. S4. Seasonal and geographic variations in the average ground acceleration power in the 50.0–100.0 second range. Energy in this bandpass is associated with flexural-gravity wave modes; i.e., a coupling of flexural A0 Lamb waves with water column buoyancy (Table S1). The faster decay of vertical power with distance from the ice front indicates the attenuation of infra-gravity waves within the sub-shelf cavity. See Fig. 6 for details.

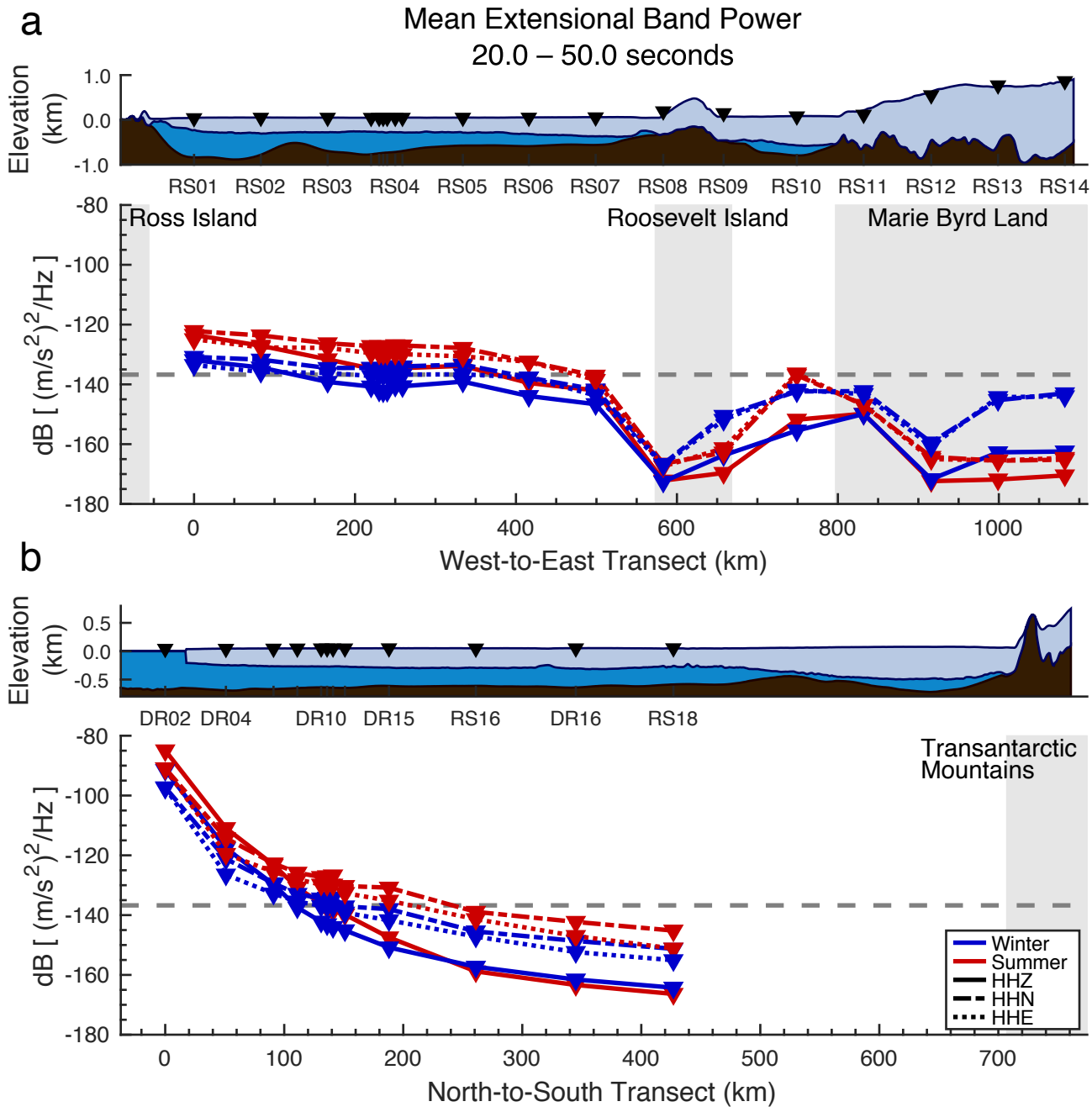

Fig. S5. Seasonal and geographic variations in the average ground acceleration power in the 20.0–50.0 second range. Energy in this bandpass is associated with longitudinally-polarized (+HOV) S0 Lamb wave modes (Table S1). See Fig. 6 for details.

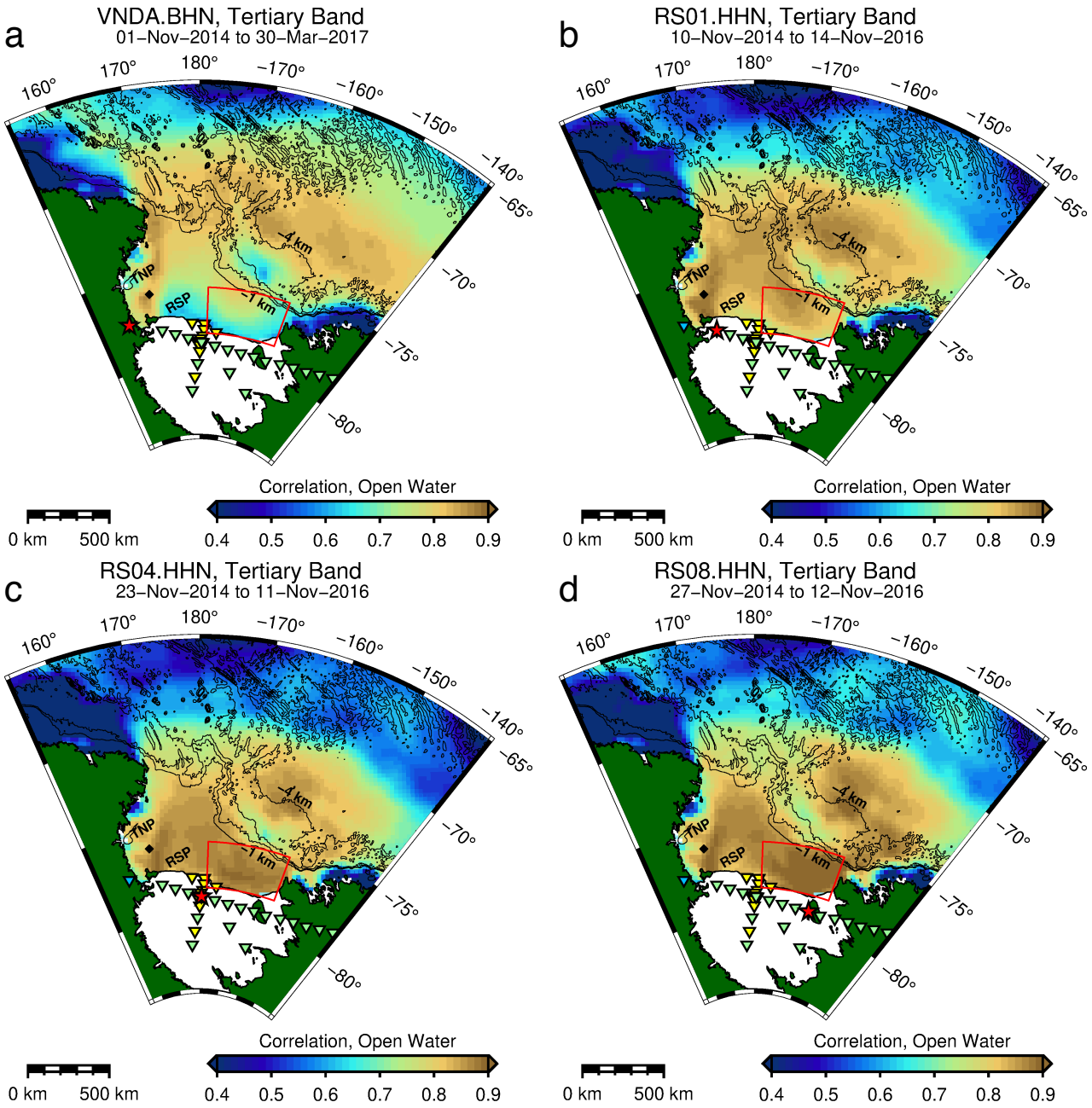

Fig. S6. North channel temporospatial correlations for the Tertiary band for an expanded selection of stations. Note the increasing correlations with proximity to the eastern Ross Sea. VNDA appears appears particularly insensitive to the Ross Sea state in comparison to the stations in the Ross Embayment. See also Figs. 9, S7.

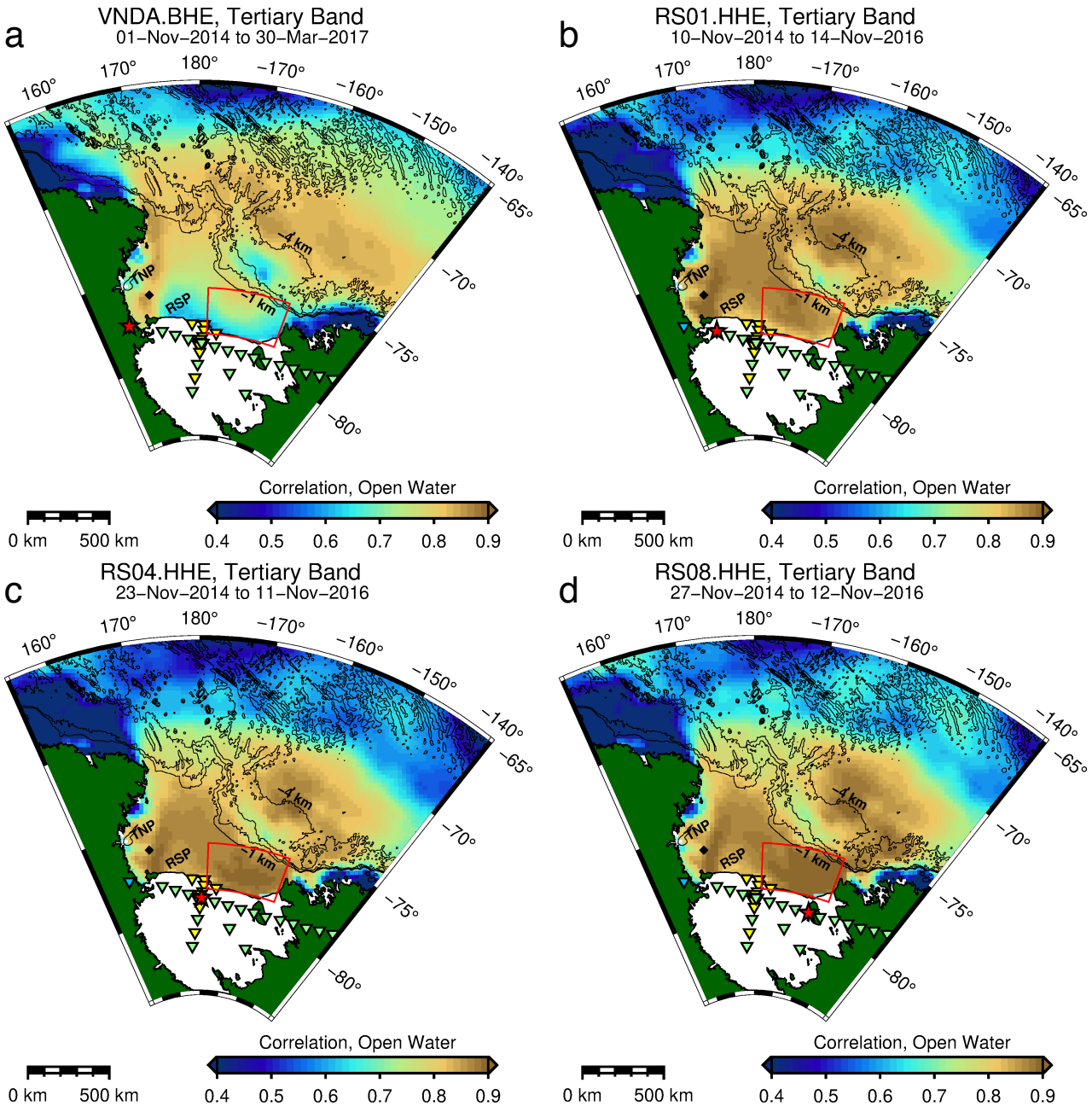

Fig. S7. East channel temporospatial correlations for the Tertiary band. See also Fig. S6.

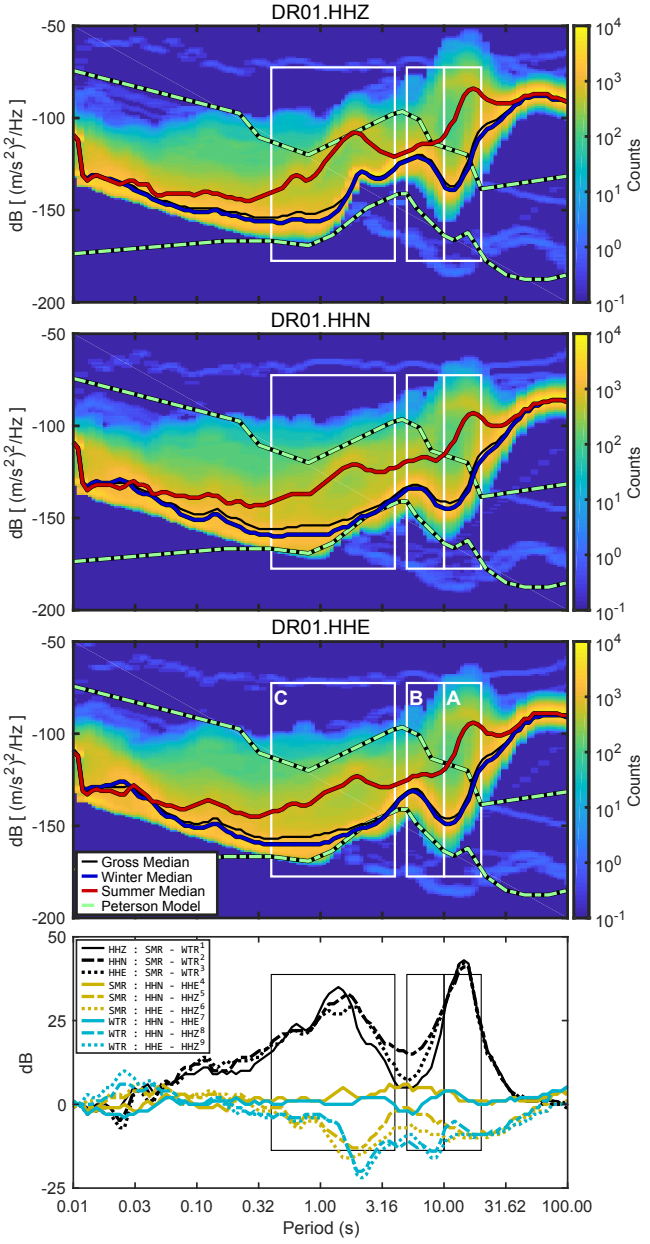

Fig. S8. DR01 PSD-PDF.

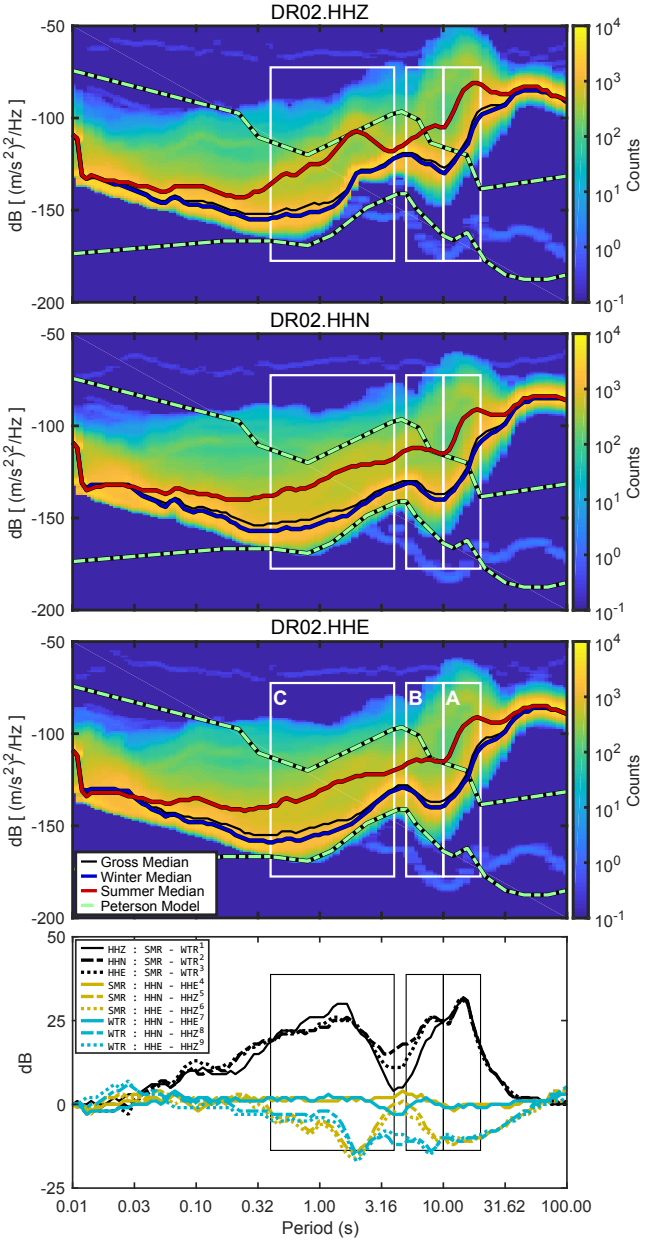

Fig. S9. DR02 PSD-PDF.

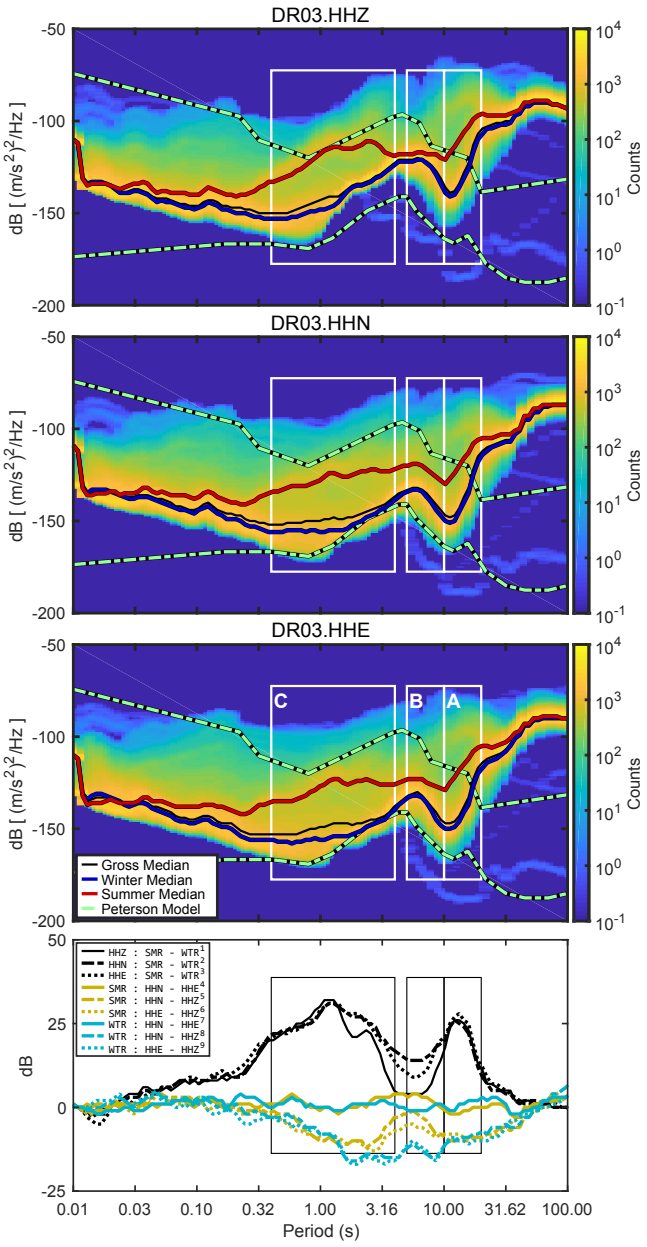

Fig. S10. DR03 PSD-PDF.

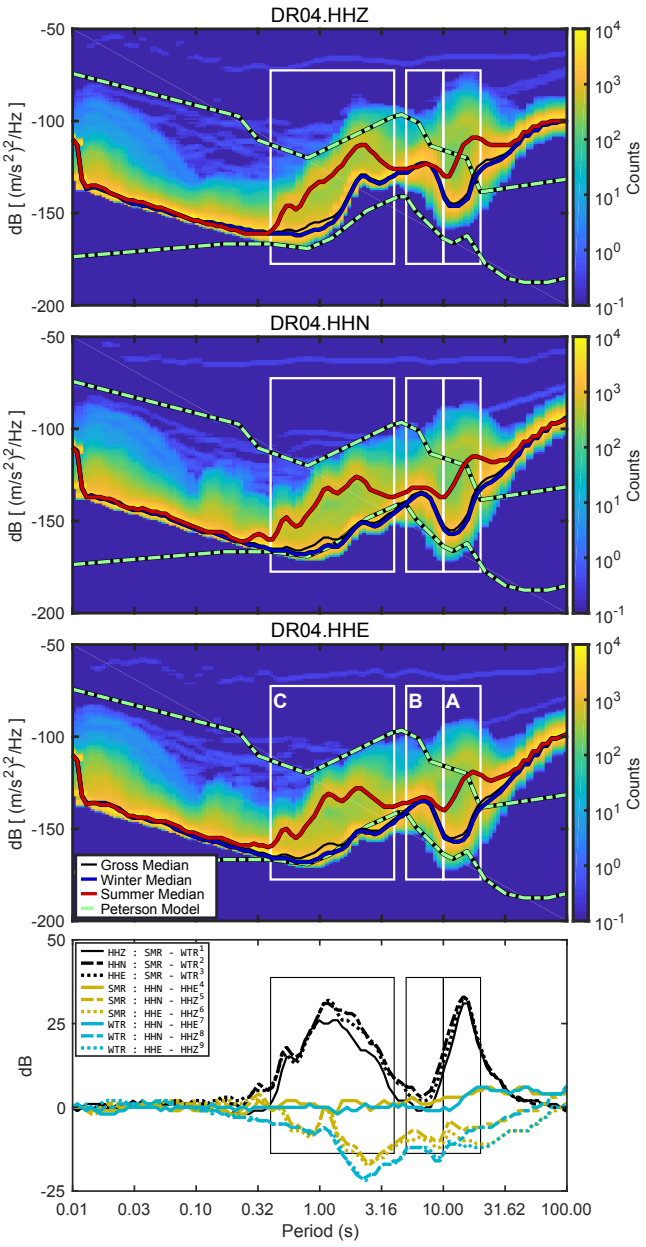

Fig. S11. DR04 PSD-PDF.

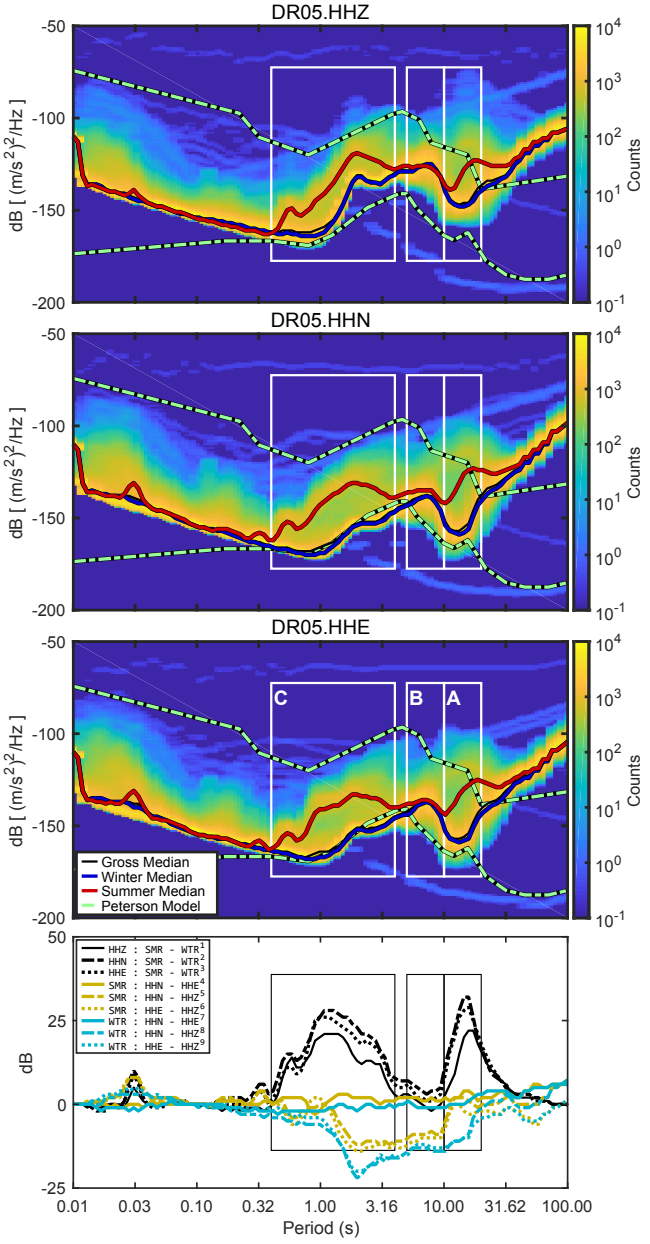

Fig. S12. DR05 PSD-PDF.

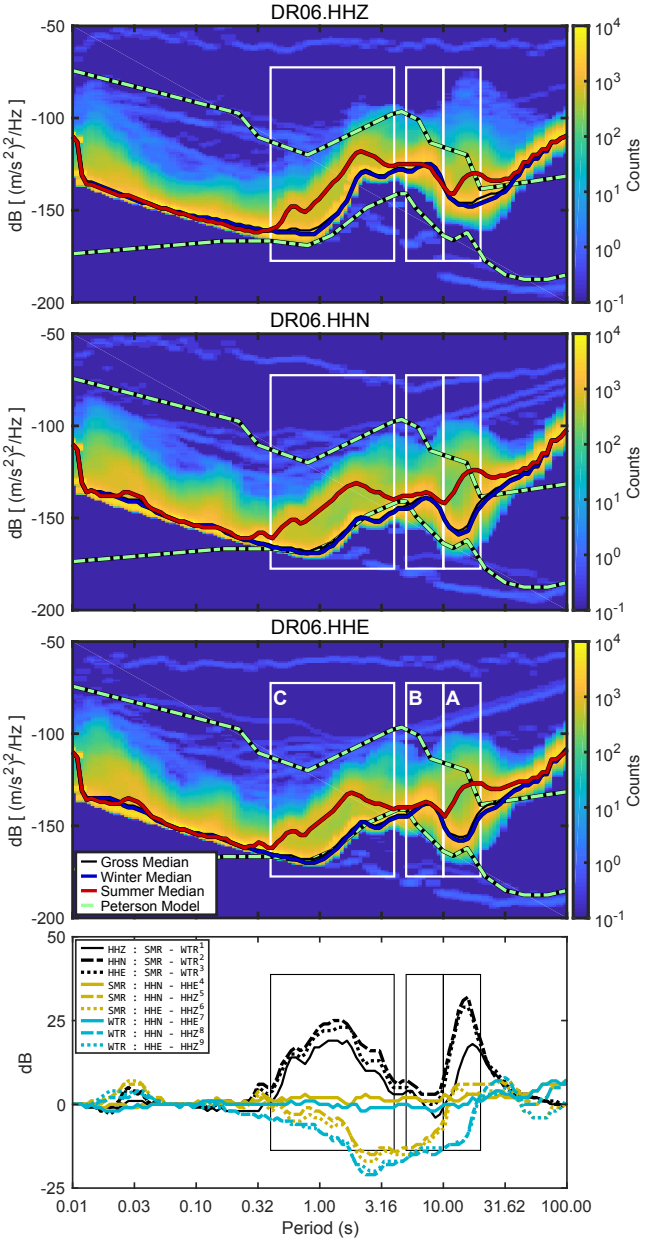

Fig. S13. DR06 PSD-PDF.

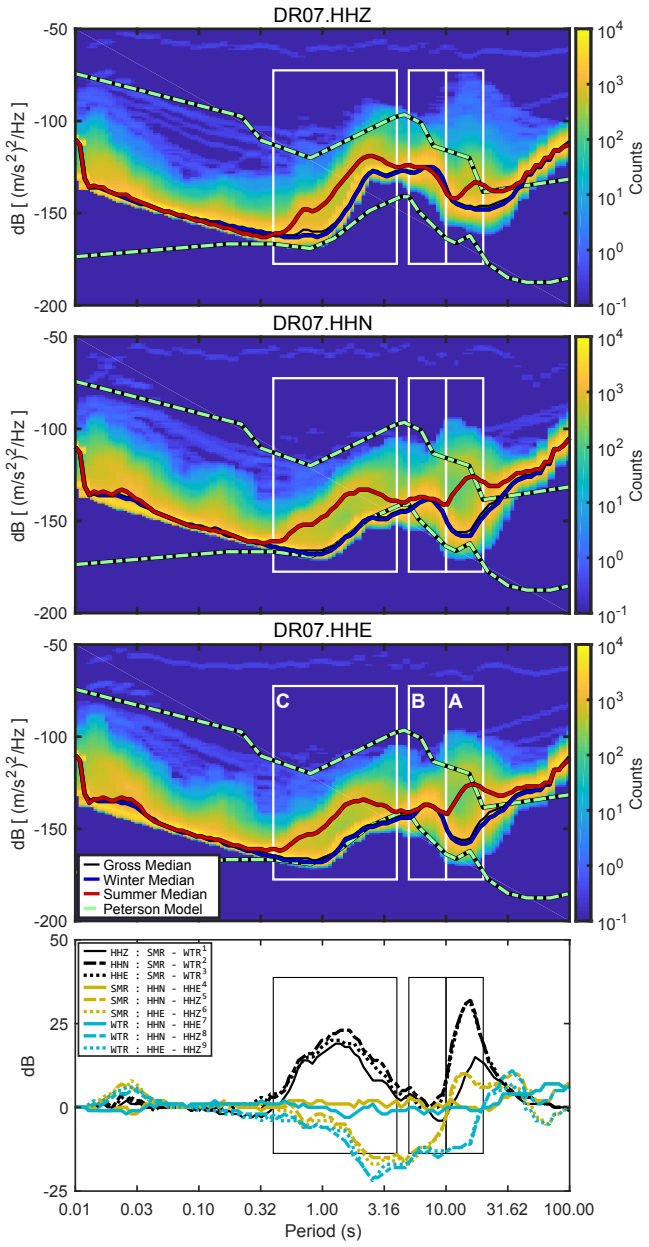

Fig. S14. DR07 PSD-PDF.

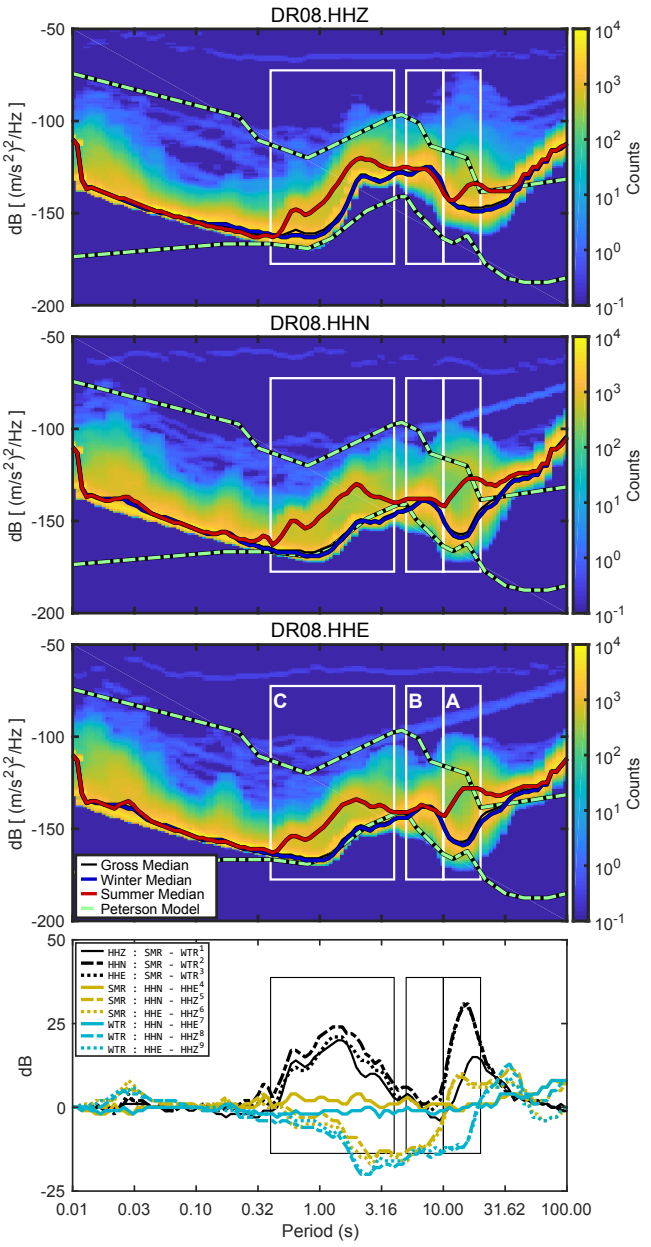

Fig. S15. DR08 PSD-PDF.

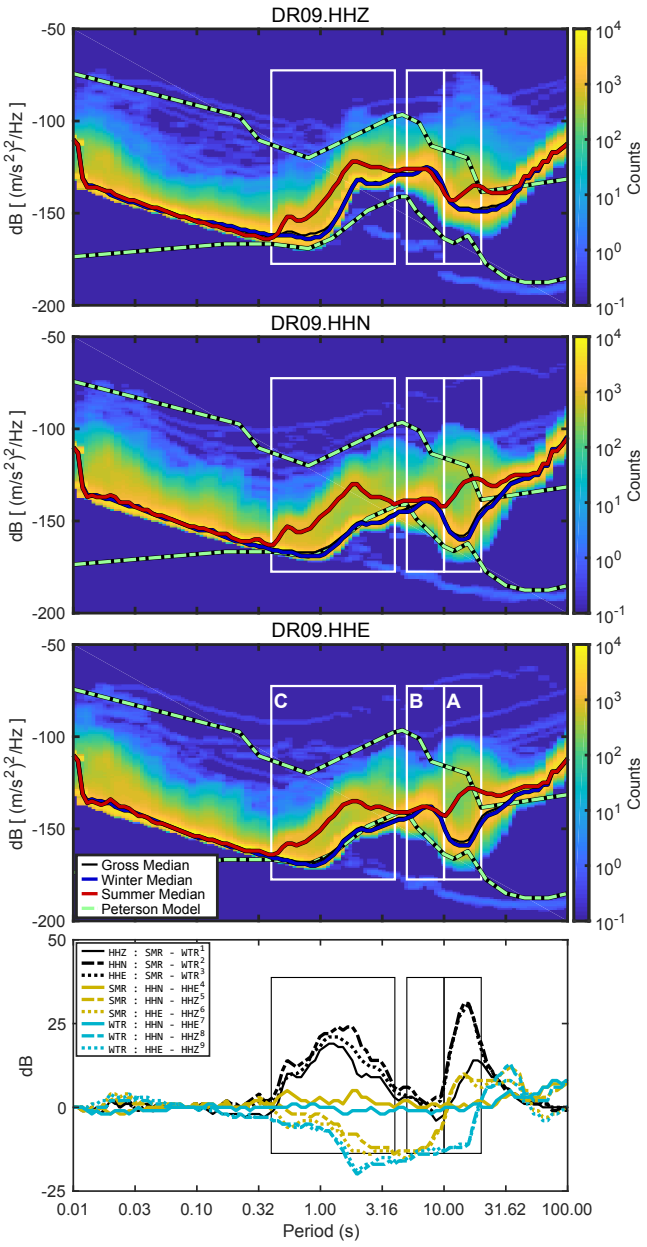

Fig. S16. DR09 PSD-PDF.

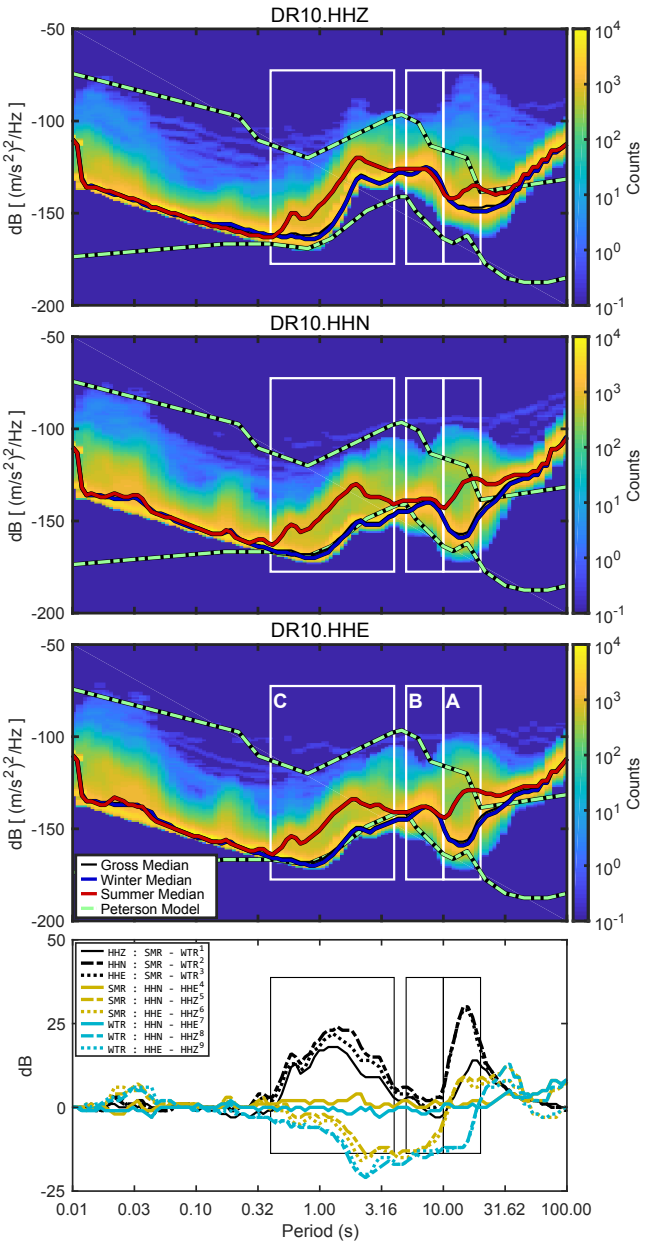

Fig. S17. DR10 PSD-PDF.

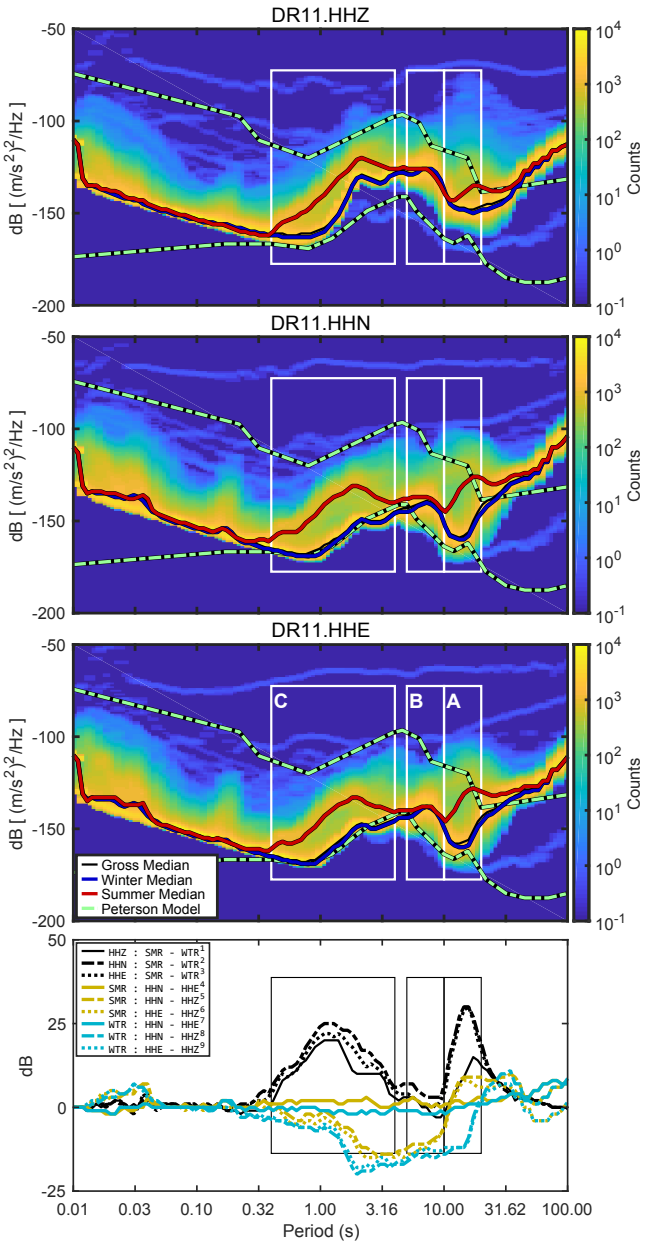

Fig. S18. DR11 PSD-PDF.

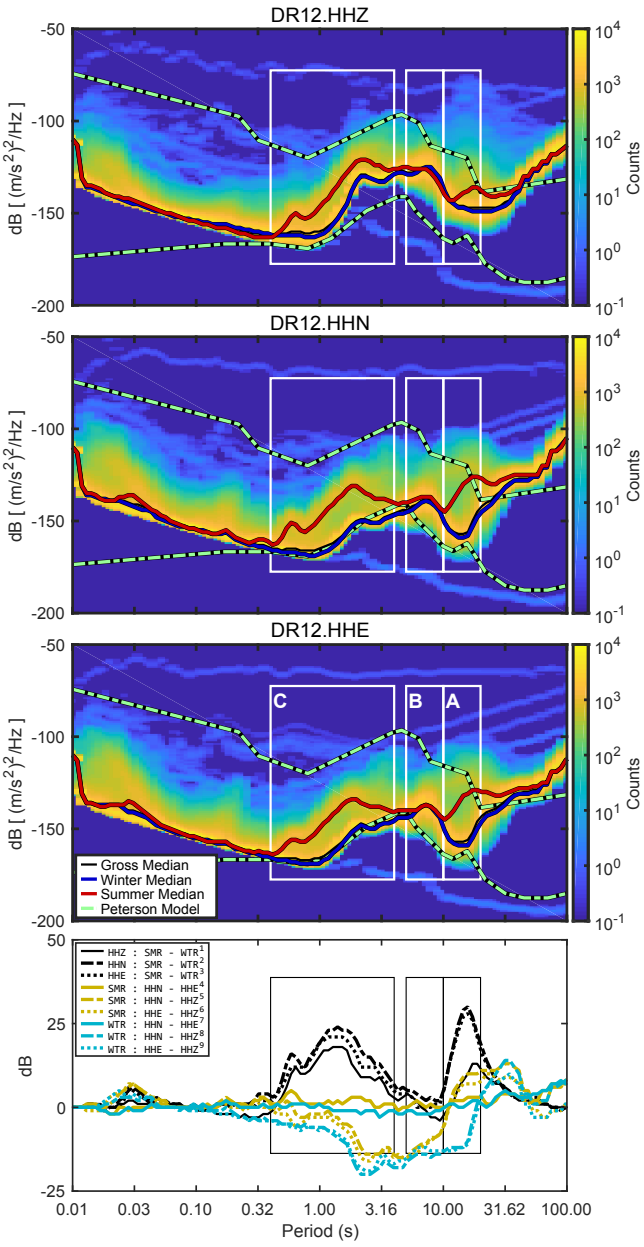

Fig. S19. DR12 PSD-PDF.

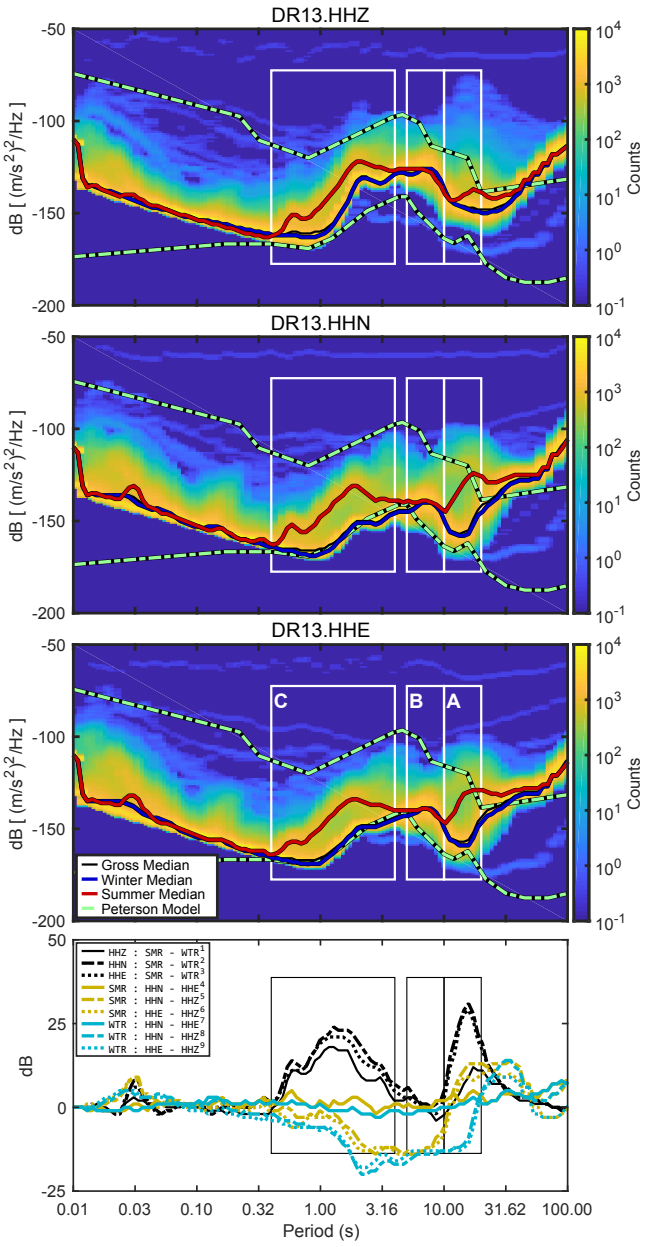

Fig. S20. DR13 PSD-PDF.

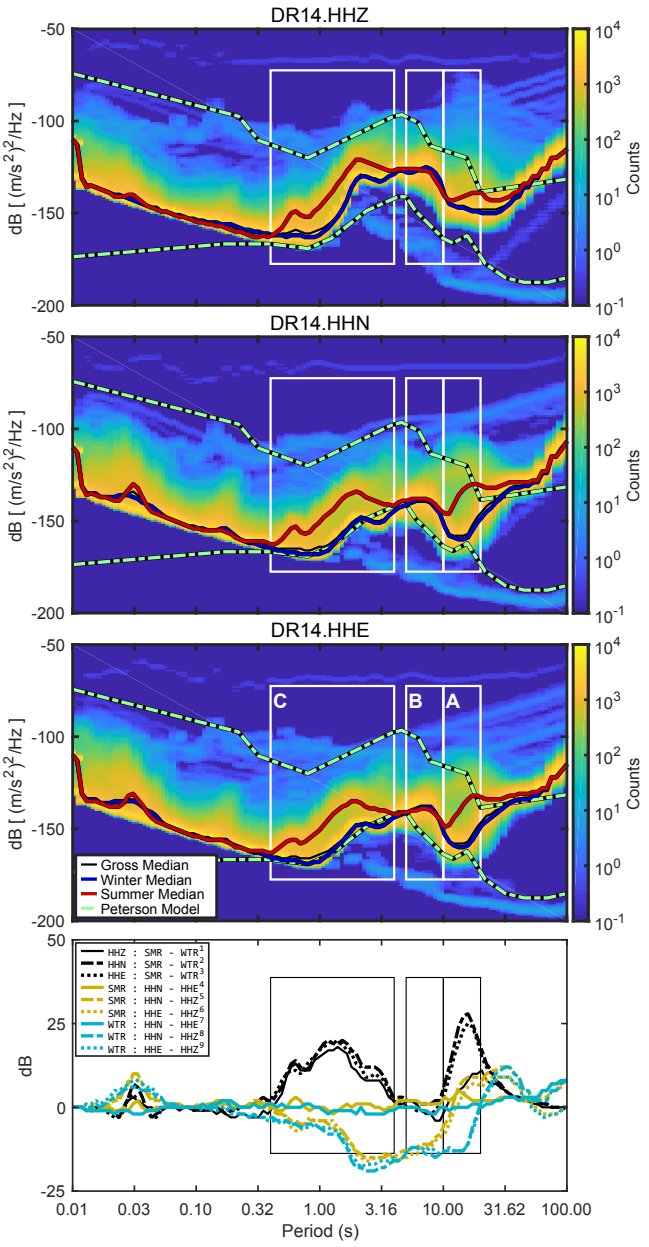

Fig. S21. DR14 PSD-PDF.

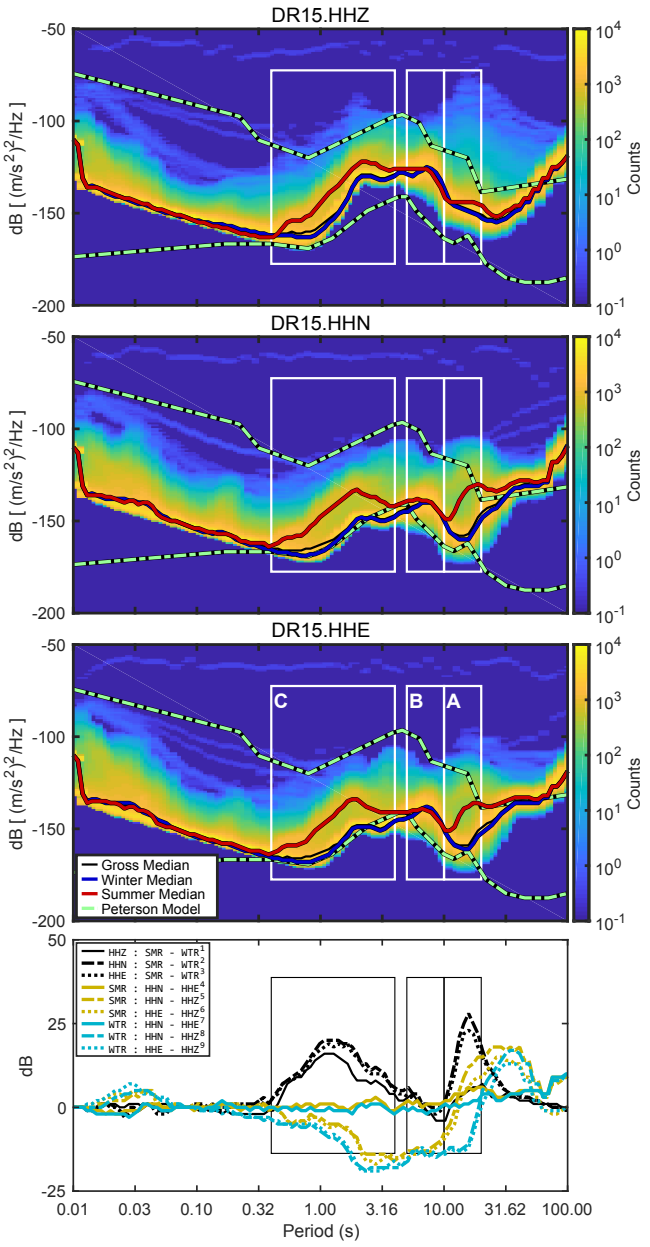

Fig. S22. DR15 PSD-PDF.

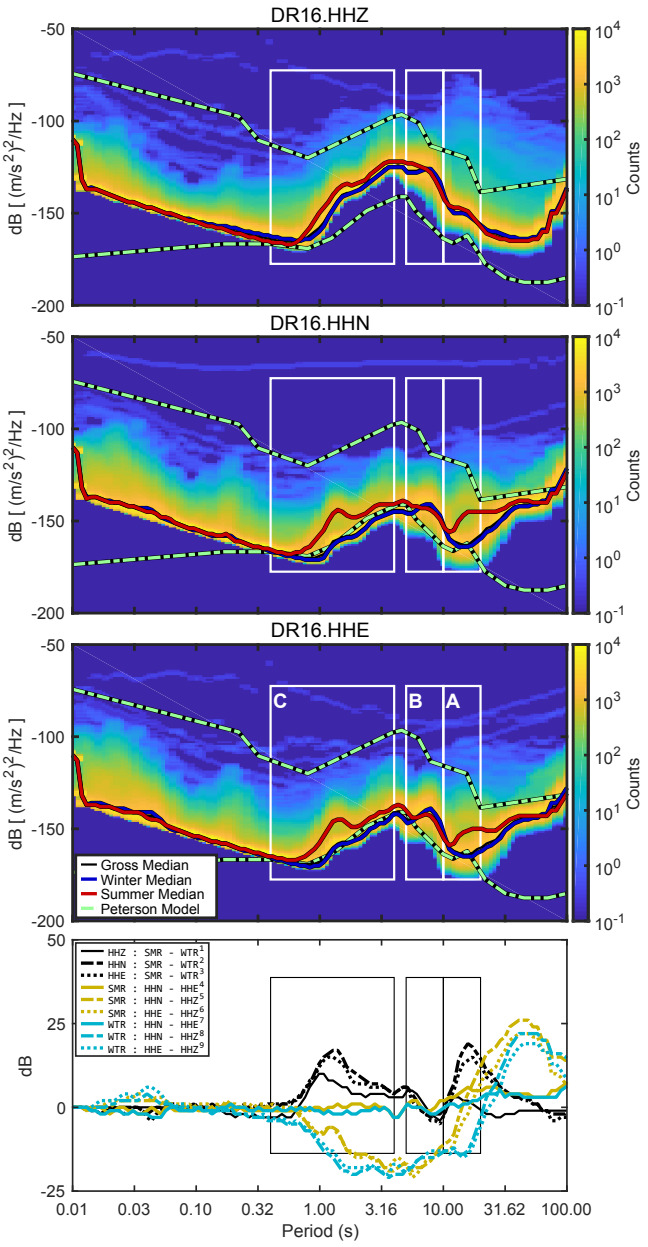

Fig. S23. DR16 PSD-PDF.

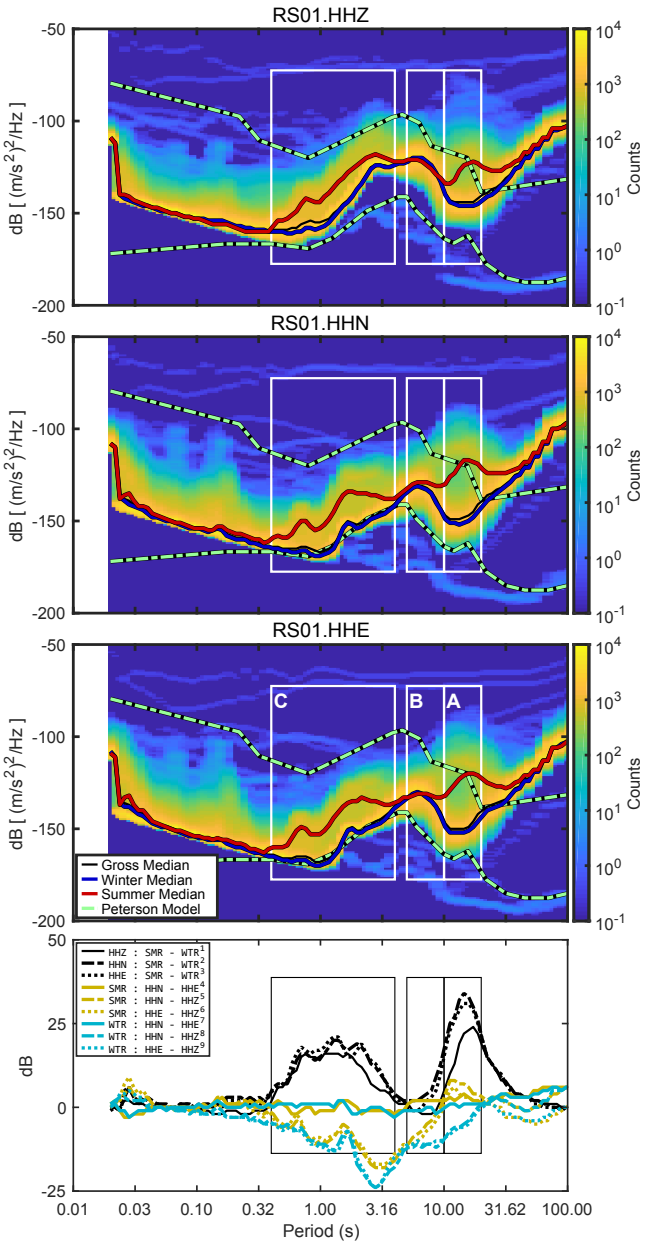

Fig. S24. RS01 PSD-PDF.

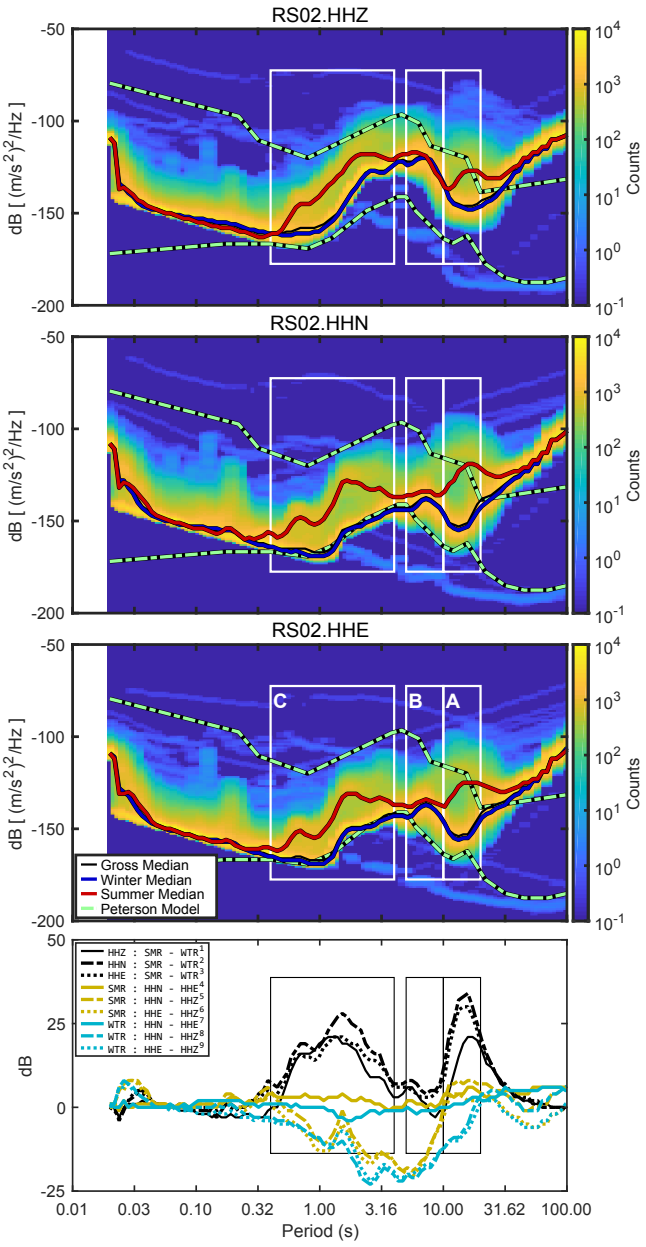

Fig. S25. RS02 PSD-PDF.

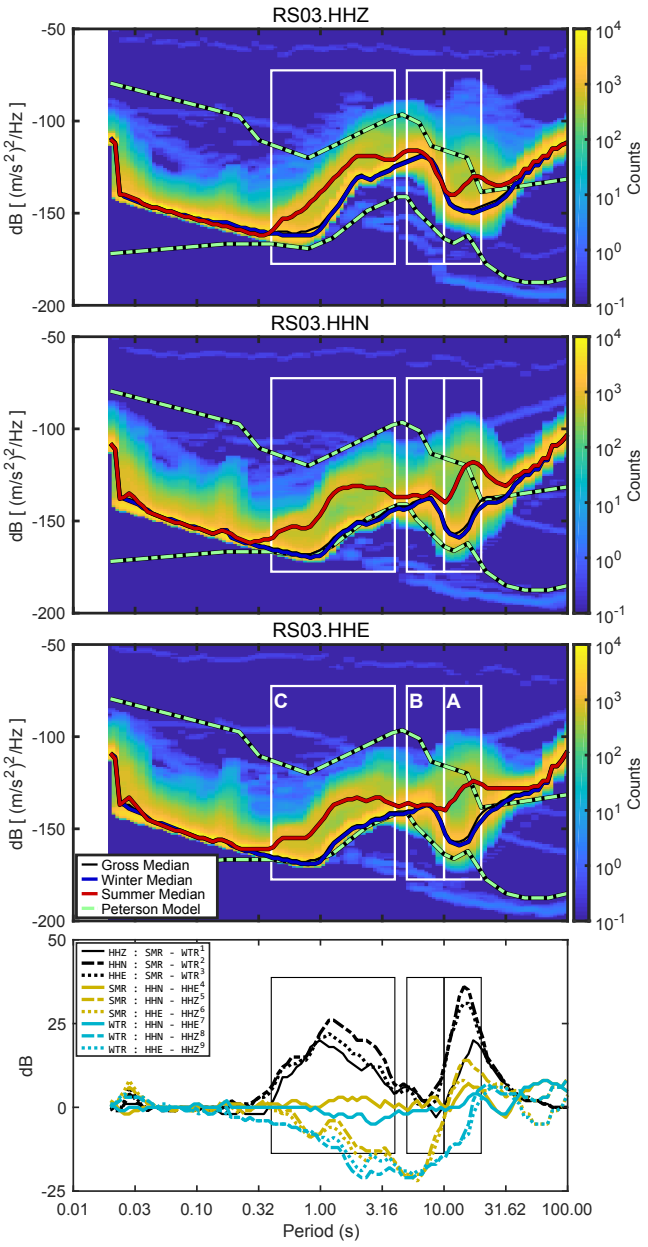

Fig. S26. RS03 PSD-PDF.

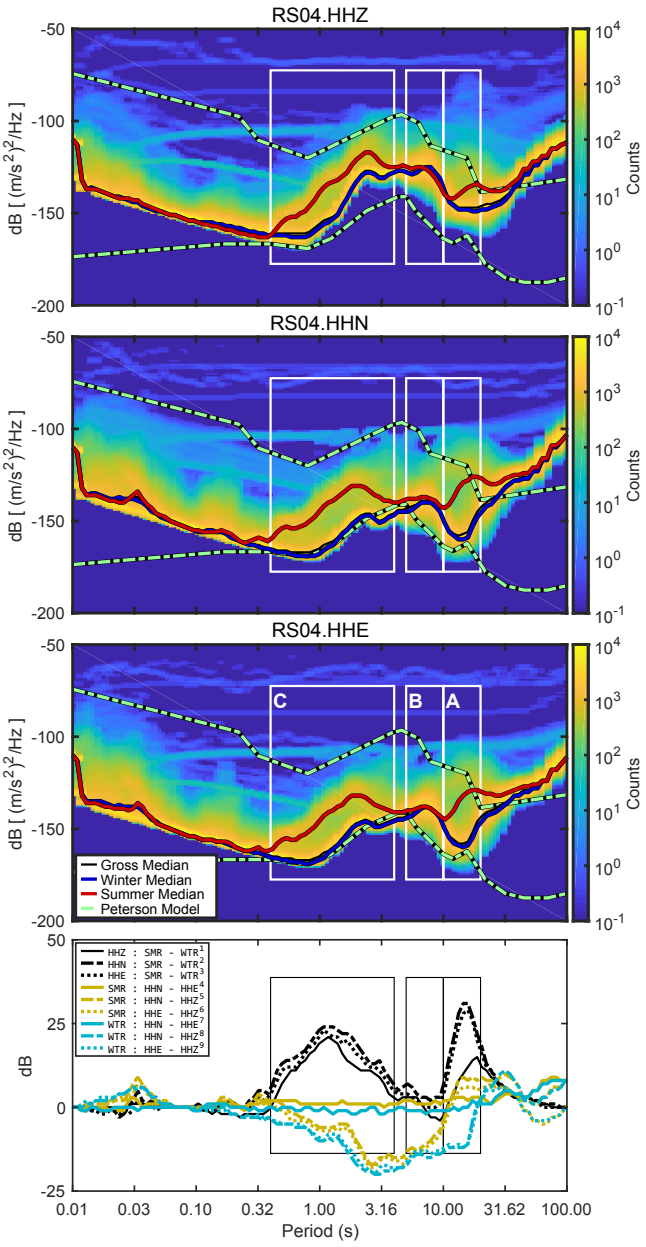

Fig. S27. RS04 PSD-PDF.

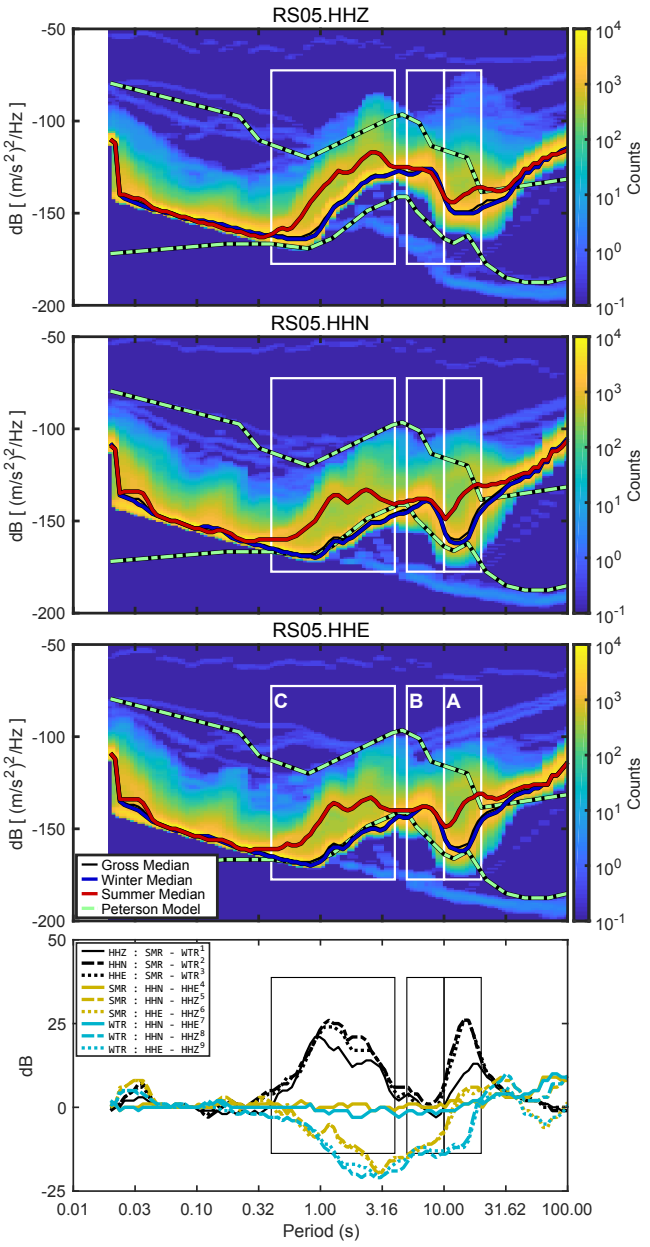

Fig. S28. RS05 PSD-PDF.

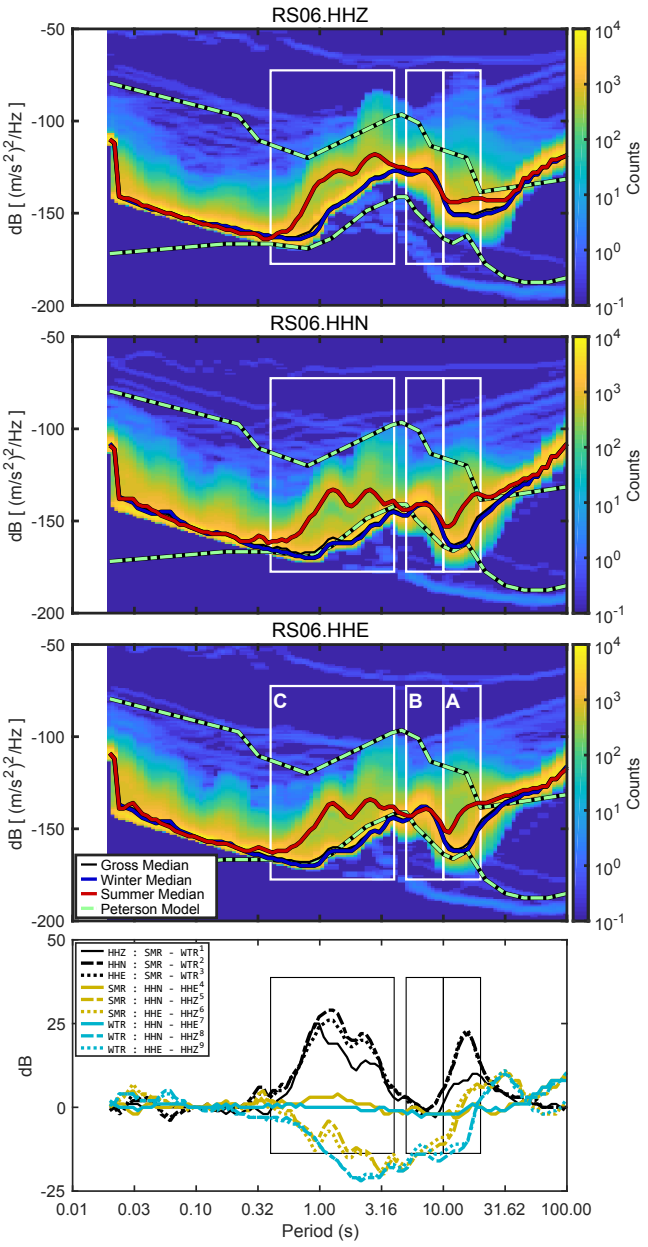

Fig. S29. RS06 PSD-PDF.

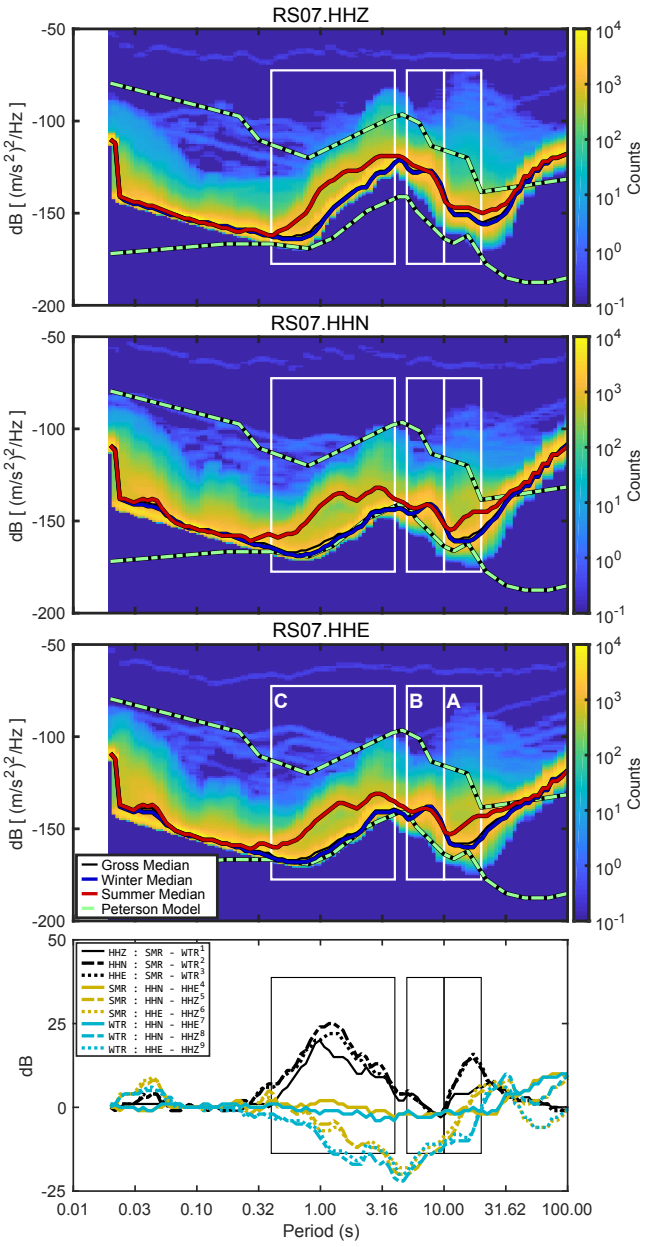

Fig. S30. RS07 PSD-PDF.

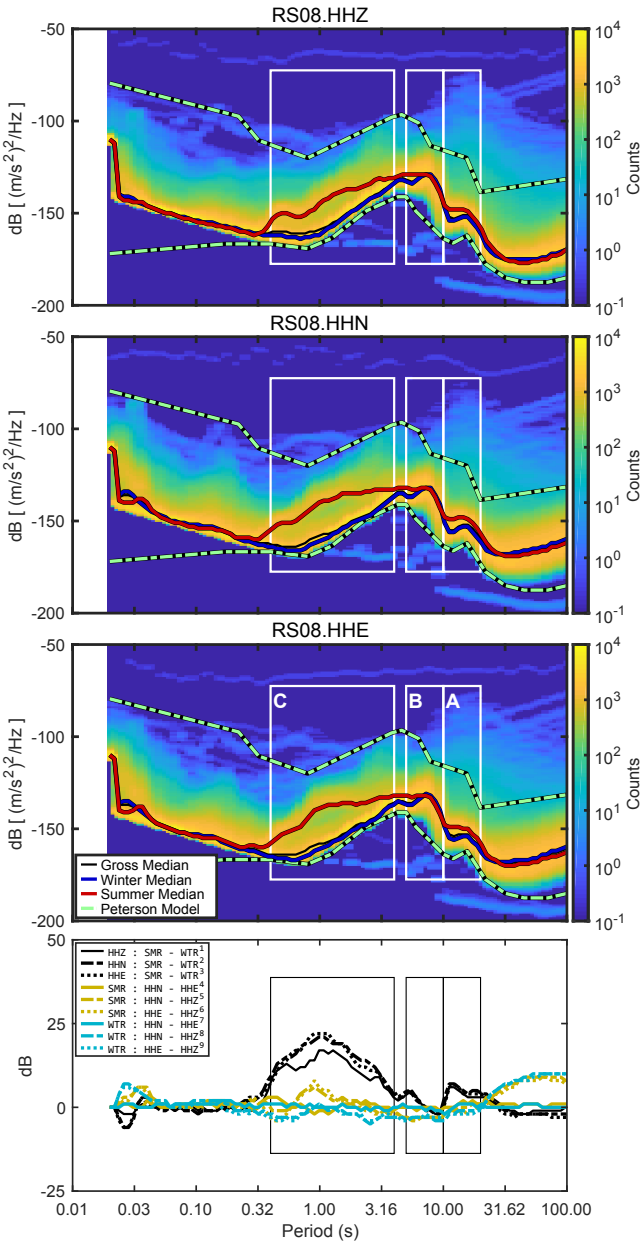

Fig. S31. RS08 PSD-PDF.

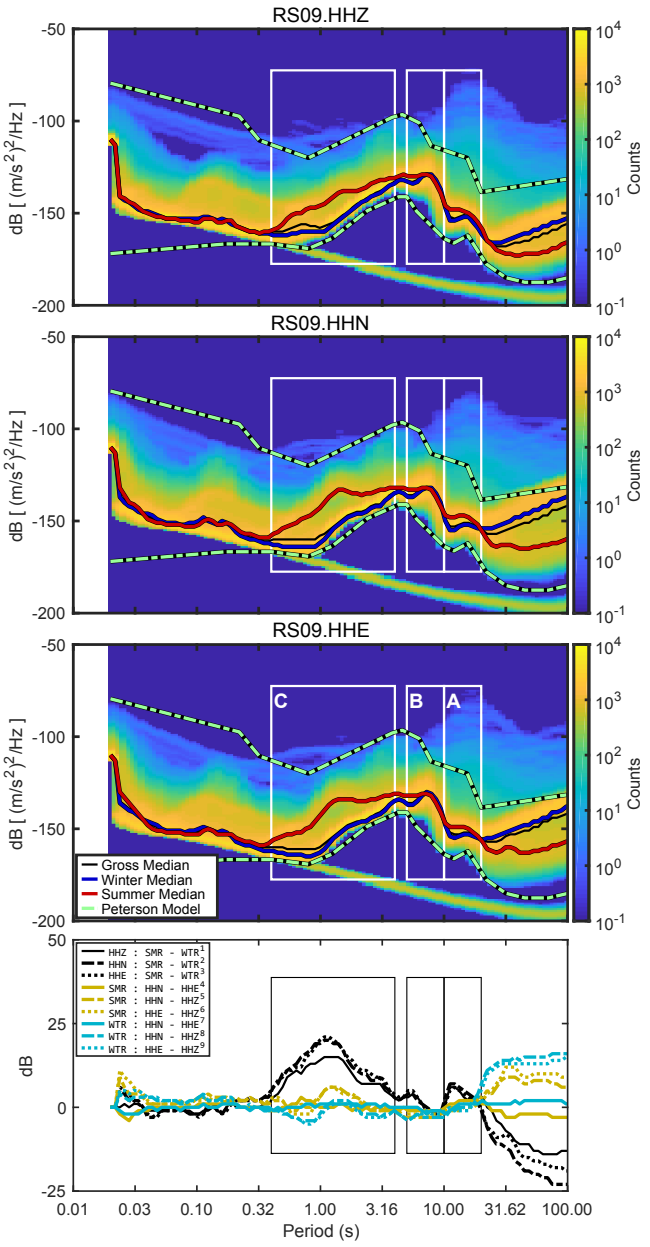

Fig. S32. RS09 PSD-PDF.

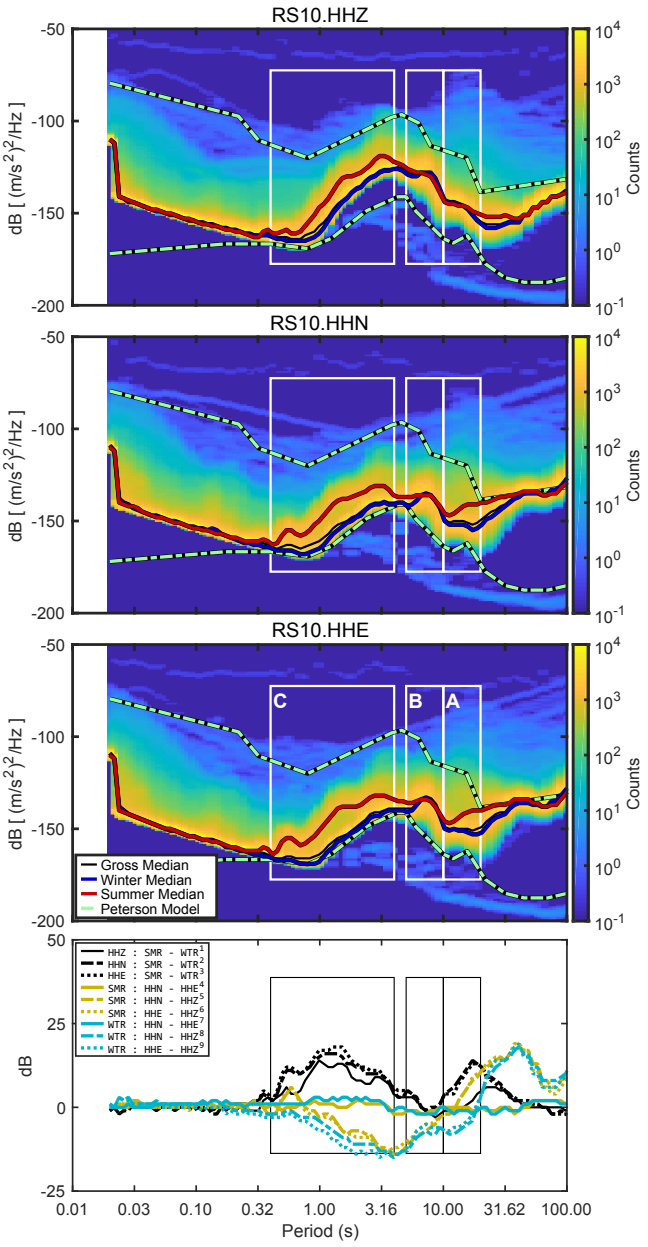

Fig. S33. RS10 PSD-PDF.

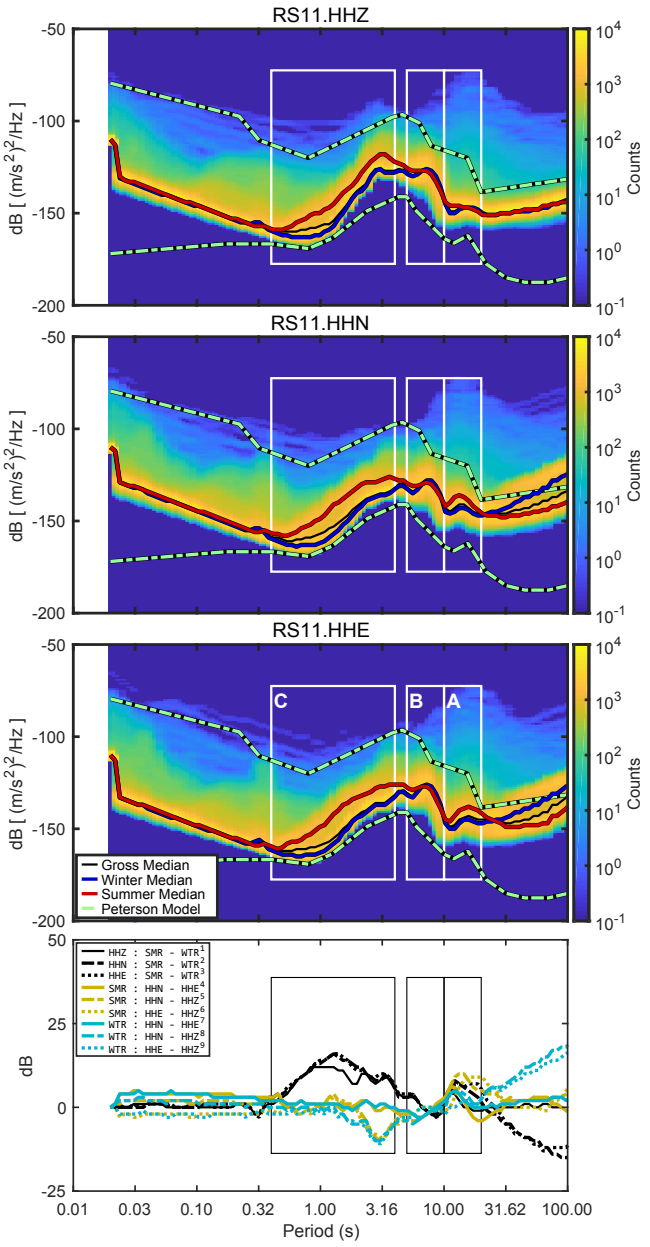

Fig. S34. RS11 PSD-PDF.

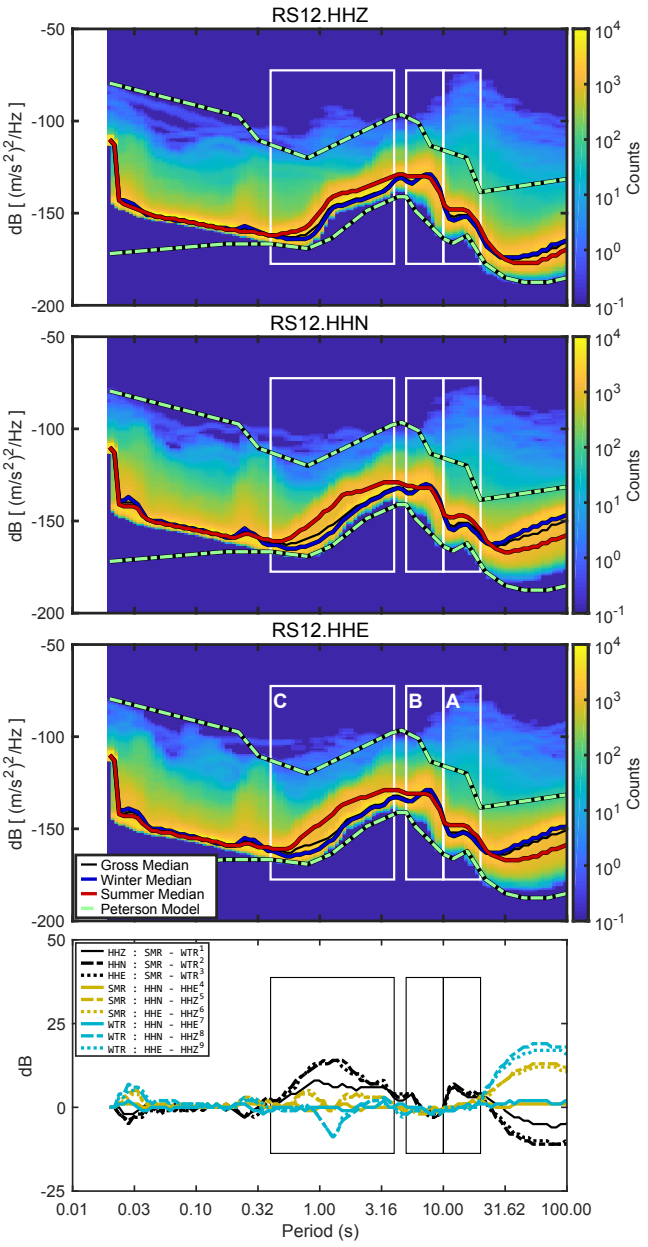

Fig. S35. RS12 PSD-PDF.

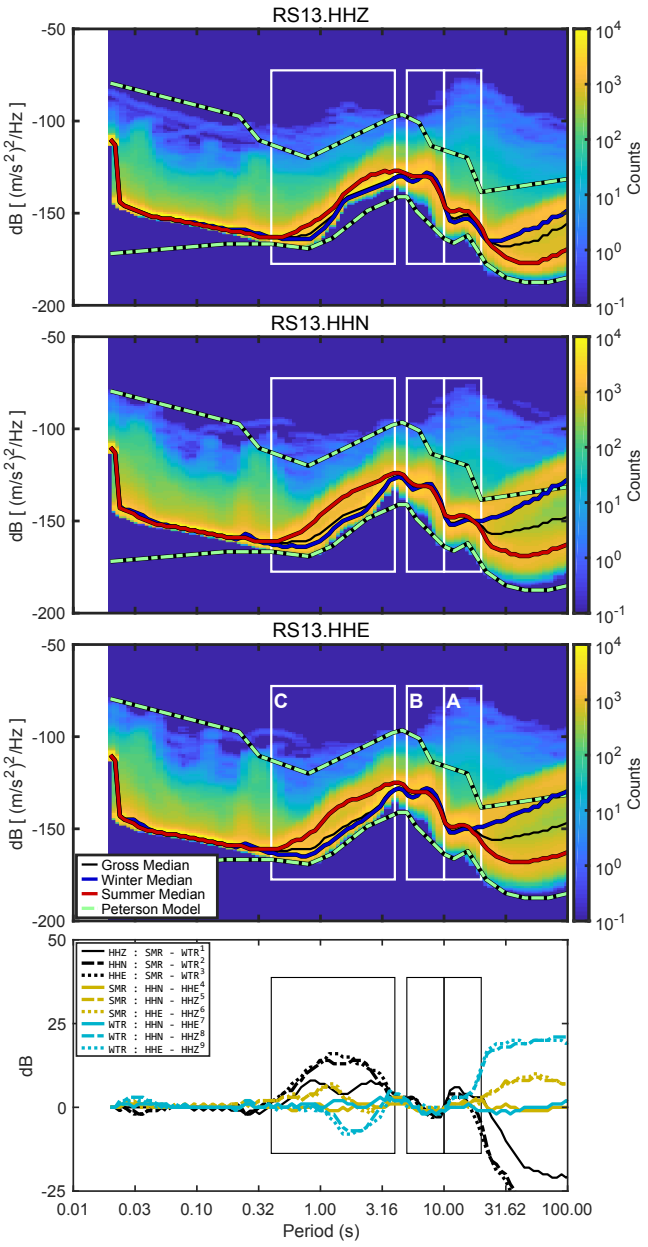

Fig. S36. RS13 PSD-PDF.

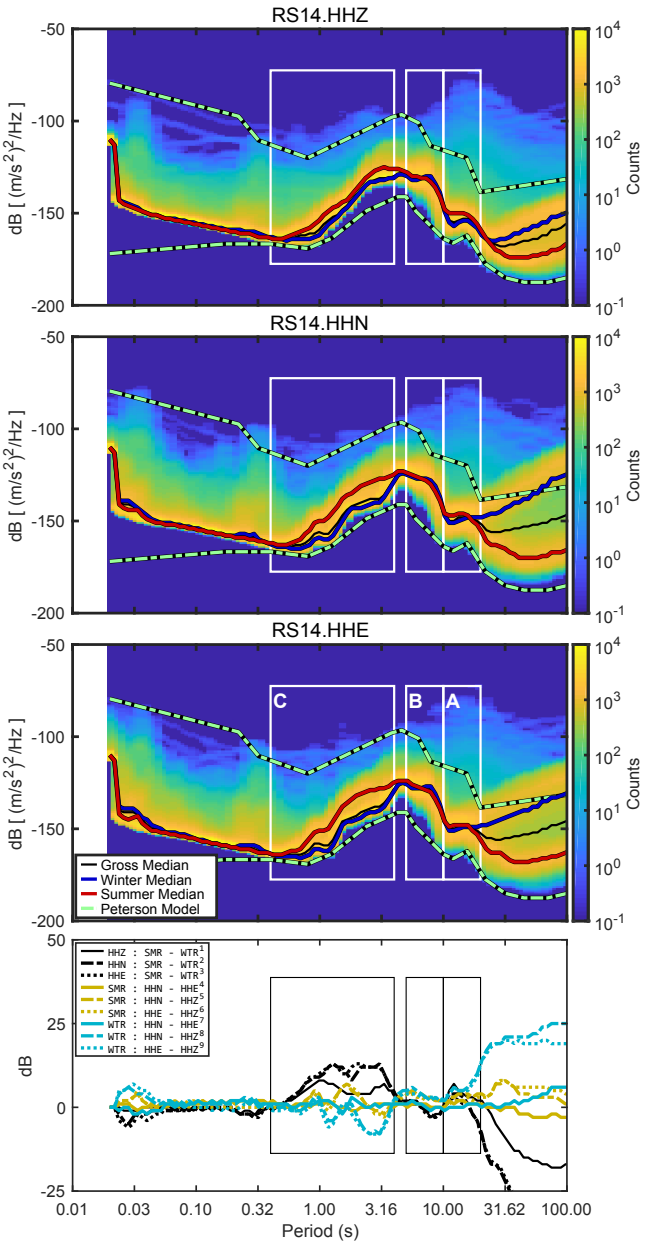

Fig. S37. RS14 PSD-PDF.

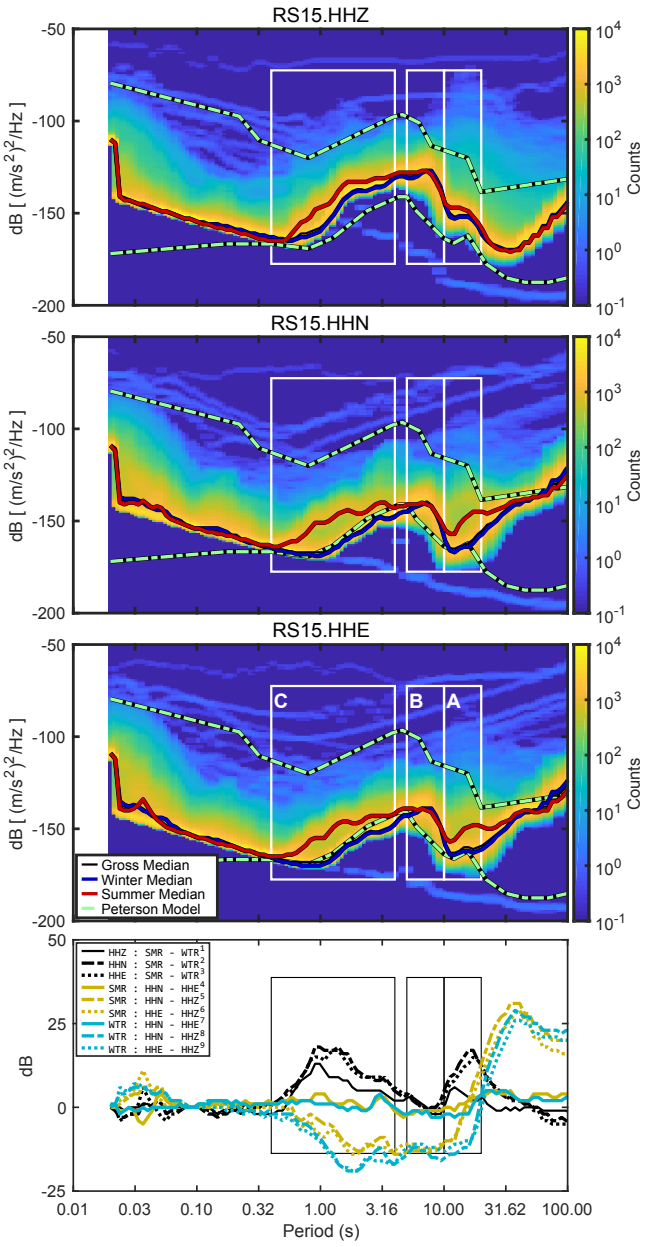

Fig. S38. RS15 PSD-PDF.

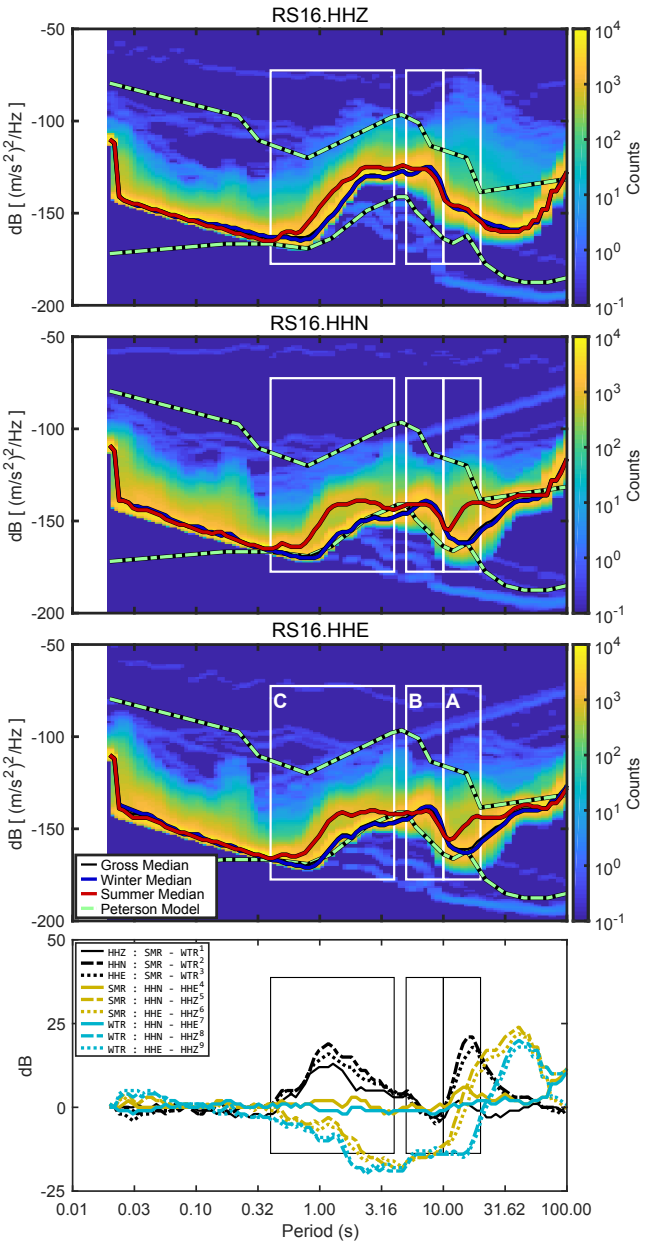

Fig. S39. RS16 PSD-PDF.

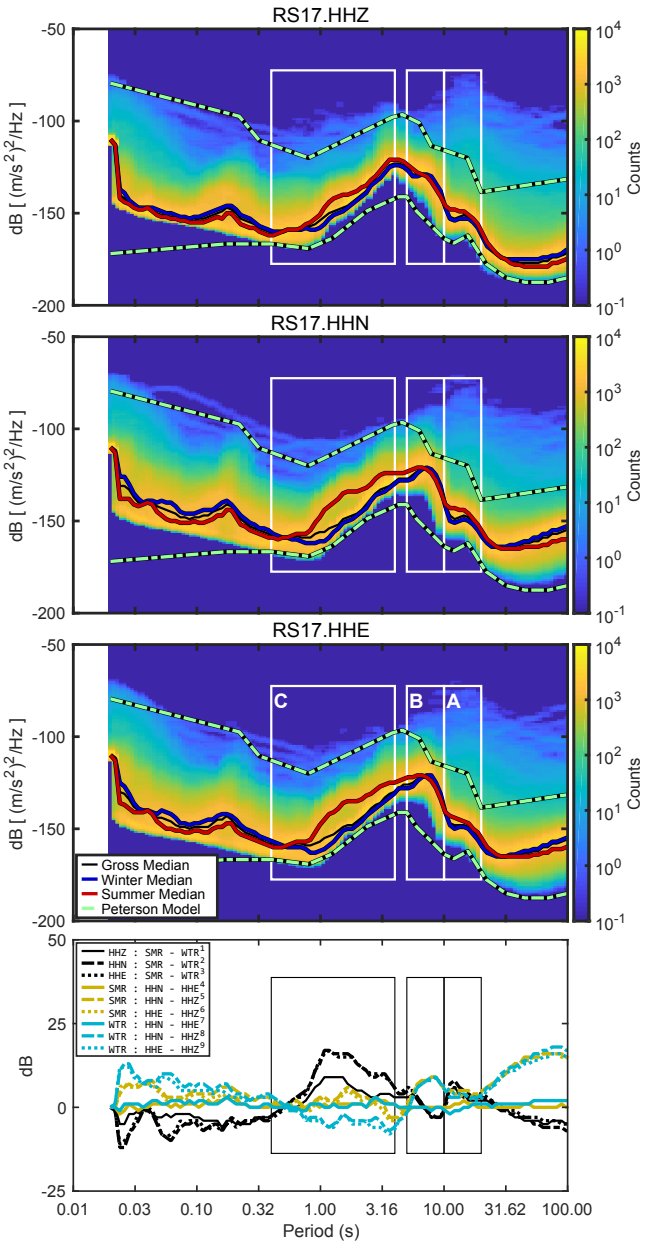

Fig. S40. RS17 PSD-PDF.

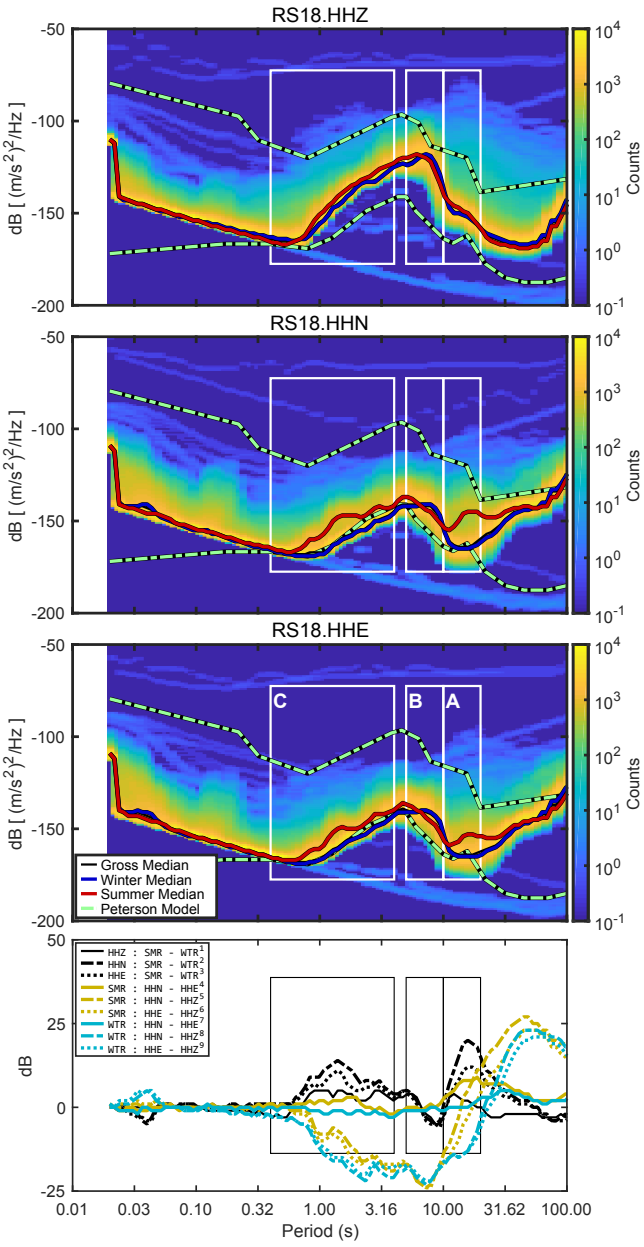

Fig. S41. RS18 PSD-PDF.

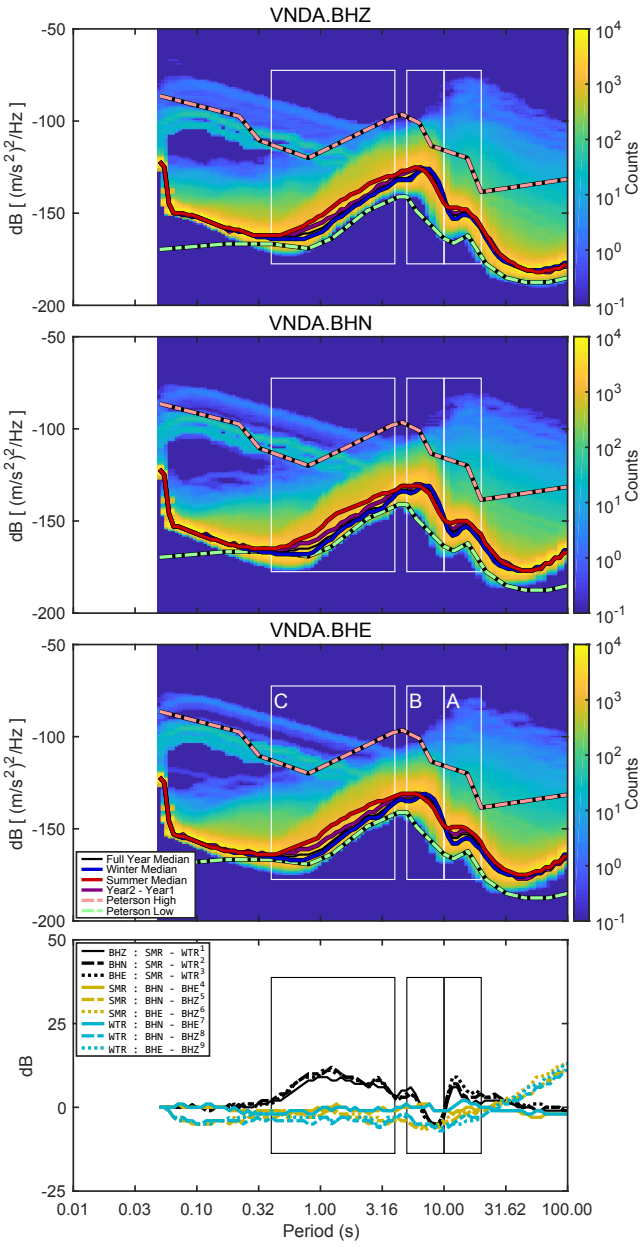

Fig. S42. VNDA PSD-PDF.

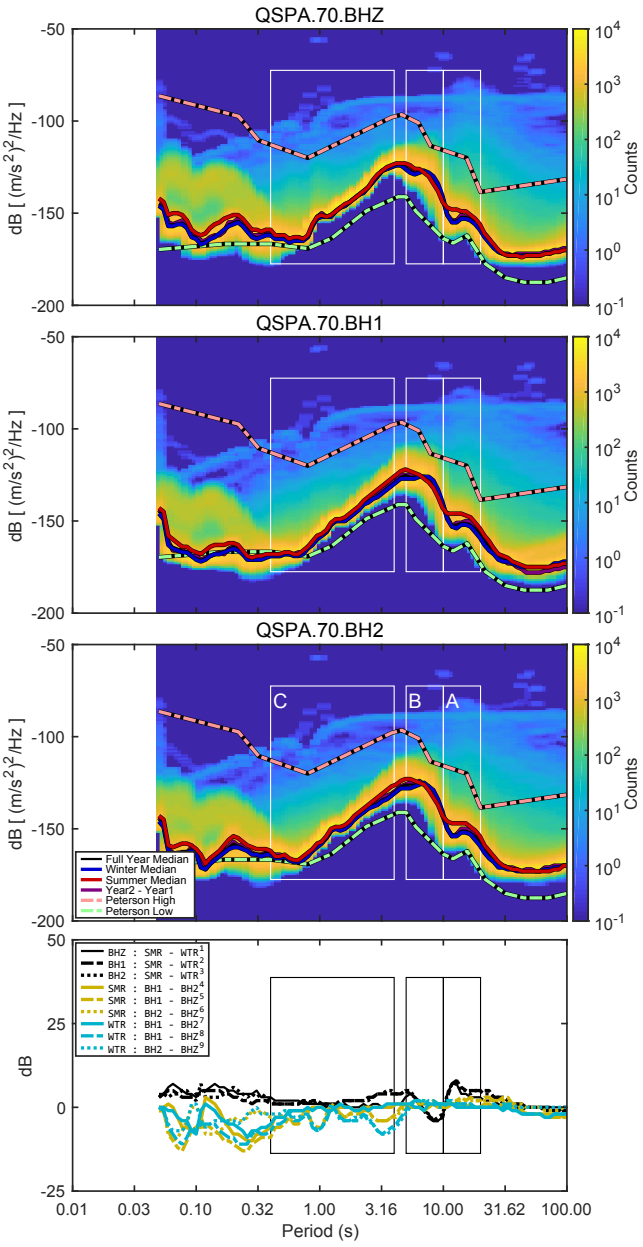

Fig. S43. QSPA Location 70 PSD-PDF.